UNIVERSITÀ DEGLI STUDI DI CATANIA
FACOLTÀ DI SCIENZE MATEMATICHE, FISICHE E NATURALI
CORSO DI LAUREA MAGISTRALE IN FISICA

SALVATORE AIOLA

Jet reconstruction in Pb–Pb collisions at $\sqrt{s_{\mathrm{NN}}} = 2.76$ TeV with the ALICE experiment

MASTER'S THESIS

Relatori:
Prof. F. Riggi
Dr. P. La Rocca
Dr. C. Loizides

ANNO ACCADEMICO 2011/2012

Contents

Chapter 1

High-energy heavy-ion collisions

1.1 Introduction

The first accelerating machines able to provide relativistic nucleus-nucleus collisions date back to the early eighties. In those years many heavy-ion experiments started their operations at the CERN *Super Proton Synchrotron* (SPS) and at the BNL *Alternating Gradient Synchrotron* (AGS). Both accelerators were first designed to collide protons, which brought some milestone discoveries, respectively the discovery of the electroweak bosons and the charm quark. Successively they were upgraded to also collide nuclei in fixed-target experiments. These experiments provided the first tantalizing evidences of a new state of matter, the "*Quark-Gluon Plasma*" (QGP).

Indeed models predict that when the nuclear matter is brought to high temperatures and/or high densities, quark and gluons, which are usually bound inside hadrons, can reach a state where they are completely deconfined and free to move in the fireball produced in the collision. Some of these models were proposed even before the theory of strong interactions, Quantum Chromo-Dynamics (QCD), was established, which provides a more natural theoretical framework to explain this new state of matter. QCD is part of the Standard Model of Elementary Particles, which also includes the Electro-Weak (EW) Theory. The Standard Model as a whole is able to describe three of the four interactions that were traditionally referred as the "fundamental forces of Nature", excluding the gravitational interaction. The Standard Model has been successfully tested by LEP experiments, which stopped operations at the end of the nineties. In particular LEP experiments were able to test the EW theory with an unprecedented and unsurpassed precision. Recently CMS and ATLAS have reported [1, 2] the observation of a new boson whose characteristics appear to be compatible with the "*Higgs boson*", which is the only missing piece of the Standard Model.

QCD is a *non-abelian* quantum field theory which is invariant under the local gauge group SU(3). There are two main physics consequences of the SU(3) group, which makes it very different from Quantum Electro-Dynamics (QED) and even from the EW theory:

Confinement The interaction between quarks does not diminish as they move apart, but conversely it grows. This is due to the self-interaction of gluons, which results in an "anti-screening" effect. In normal hadronic matter, quarks are bound together. It is interesting to see what happens when one tries to separate them, e.g. in Deep-Inelastic Scattering (DIS) experiments. The empty space between the two separating quarks is full of virtual quark pairs and gluons and at a certain point the energy of this system is large enough that it becomes energetically more favorable to create a quark-antiquark pair than to move the two original quarks further apart. This process goes on until the energy of the system becomes too low to produce new particles and other low-energy processes start (e.g. particle decays). For this reason

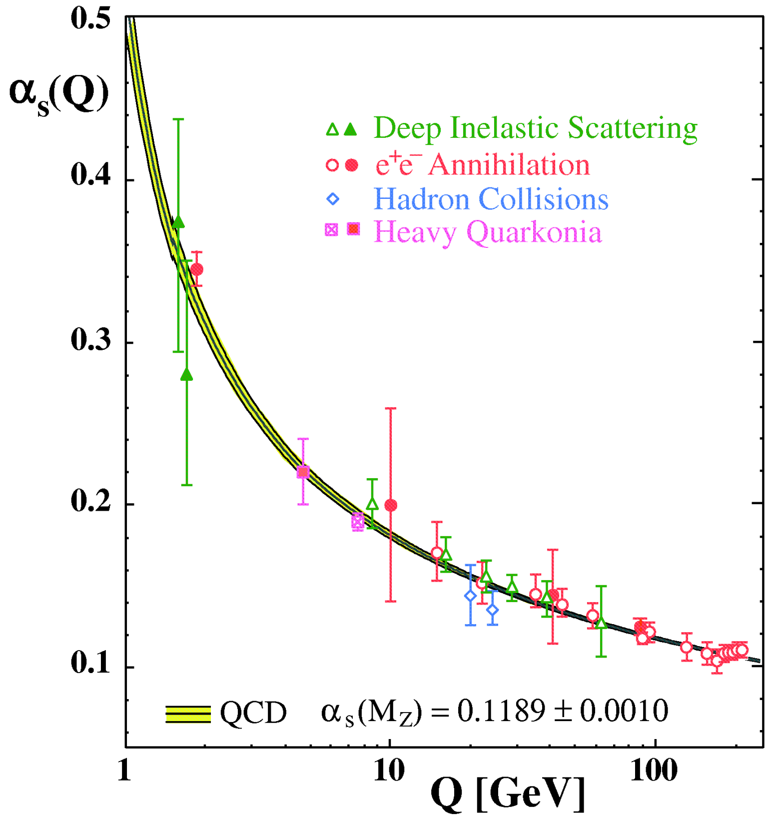

Figure 1.1: Summary of measurements of $\alpha_s(Q)$ as a function of the respective energy scale Q. The curves are the QCD predictions for the combined world averaged experimental values [3].

quarks and gluons are never observed freely, but always bound inside a hadron. The whole process is called "hadronization" and it gives the theoretical grounds to explain hadron production in all kinds of particle collisions (ep, e^+e^-, pp, ...). In particular it is the basis of the jet production in high-energy collisions, where, after a high momentum transfer between two partons, the hadronization process can give rise to a collimated spray of particles, called "jet", which, to some extent, follows the kinematics of the original scattered parton and its partonic QCD showering.

Asymptotic freedom At very high energy QCD predicts that the interaction between quarks and gluons becomes weaker. This is what happens in the QGP: in the hot and dense medium, the energies of quarks and gluons are high and the distances between them very small, thus the interactions are reduced and they move almost freely in the fireball.

Both the confinement and the asymptotic freedom are explained in terms of a "running" coupling constant α_s, as a function of the momentum transfer Q^2:

$$\alpha_s(Q^2) = \frac{12\pi}{(11N_C - 2N_f)\ln\left(\frac{Q^2}{\Lambda_C^2}\right)}, \tag{1.1}$$

where N_C is the number of "colors" (the charges of QCD theory), N_f is the number of EW flavors and Λ_C is the scale parameter of the QCD, lying between 100 MeV and 500 MeV. The "running" of the α_s coupling constant is shown in fig. 1.1.

1.2 The Quark-Gluon Plasma

1.2.1 Formation and evolution of the QGP

The geometry of a nucleus-nucleus collision is sketched in fig. 1.2. The two nuclei, traveling in opposite directions along parallel trajectories, appear to be compressed along the direction of motion because of the relativistic Lorentz contraction. During the collision they deposit a large amount of energy in a very small volume.

In peripheral collisions only the nucleons in the overlapping region will partecipate in the collision. These are called participant nucleons, while all the others, called spectators, continue their motion along

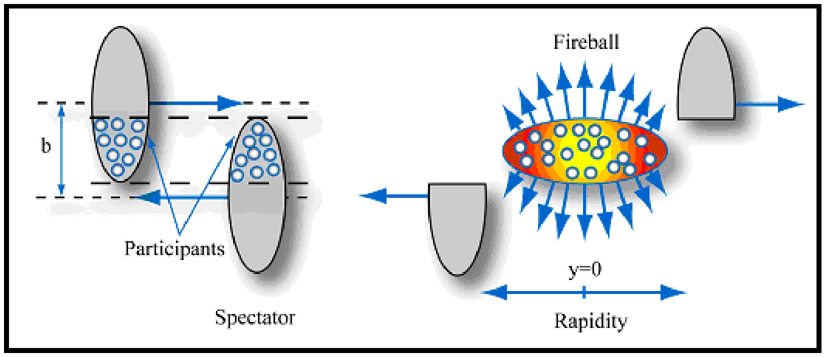

Figure 1.2: Geometry of a high energy nucleus-nucleus collision.

their original trajectory. The head-on collisions, in which the impact parameter is very small and the number of participants is equal to the total number of nucleons, lead to the highest energy density. Indeed the determination of the collision centrality is an important task as the characteristics of the *fireball*, like its energy density, shape, etc., will mostly depend on it. The fireball is the resulting hot and dense matter created in the collision. The formation of the QGP in the fireball is expected when the energy density reaches a certain critical value, which has been estimated to be ~ 1 GeV/fm^3. The quark-gluon plasma can also be created by "heating" the hadronic matter. In fact if the temperature is increased the hadrons "melt", deconfining their quarks and gluons. The phase transition can thus be achieved by increasing the temperature, the baryonic density or both of them. As a consequence, we can characterize the state of the hadronic matter by a phase diagram in the (T, μ_B) plane, where T is the temperature of the system expressed in MeV and μ_B is the barionic chemical potential[1]. As the temperature increases, the coupling between quarks becomes smaller,

[1]The baryonic chemical potential μ_B of a system is defined as the change in energy E of the system when the total baryonic number N_B (baryons – antibaryons) is increased by one unit: $\mu_B = \frac{\partial E}{\partial N_B}$.

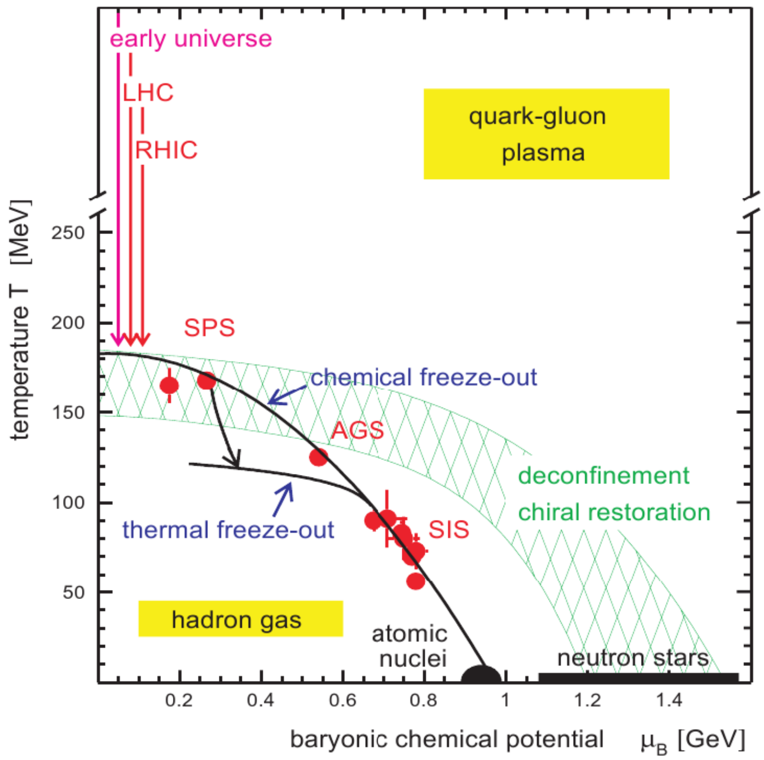

Figure 1.3: QCD phase diagram in the (T, μ_B) plane. The green area indicates the expected phase transition region within its present uncertainty. Transitions provided by various heavy ion experiments are indicated.

leading to deconfinement of the quarks. The critical temperature for $\mu_B \approx 0$ (LHC energies) is $\sim$ 170 MeV. Chiral symmetry restoration (the quarks appear as nearly massless particles) is also expected. This new state of matter is indicated in fig. 1.3 above the curved line.

After a short equilibration time τ_0 the QGP state reaches thermodynamical equilibrium. The system behaves like a fluid, and indeed the subsequent evolution of QGP is usually described in terms of its hydrodynamical properties.

The fireball created in the heavy-ion collisions expands because of its high internal pressure, while lowering its temperature. Finally it reaches the critical temperature again, thus leading to a phase transition back to normal hadronic matter. It evolves toward a hadron gas phase, in which thousands of hadrons are produced and interact through both elastic and inelastic processes. Eventually the temperature decreases at a point where inelastic interactions between the hadrons stop. The particle ratios are fixed at this point and we refer to this transition as *chemical freeze-out*, meaning that the "chemical" composition, i.e. the particle abundances, is no longer altered. After further expansion and cooling the elastic interactions are stopped so that the momentum and energy distributions of the produced particles are fixed as well. We refer to this state as a *thermal freeze-out*.

1.2.2 QGP, astrophysics and cosmology

The study of the QGP has also some astrophysical and cosmological interests. Indeed there are at least two situations in astrophysics and cosmology where the QGP phase could be relevant: compact stars (e.g. neutron stars) and the early Universe.

The early stages of the evolution of the Universe are described by the well established Big Bang scenario, which is based on a number of empirical observations. Hadrons were formed in the quark-hadron transition when the Universe was about 10^{-5} seconds old. The temperature was then about 200 MeV. Before this transition, all matter in the Universe was contained in a small region with an enormous density, a QGP. This is not the only phase transition which is believed to happen in the very early stages of the Universe, but it is the only one which is reproducible in a laboratory with the current technologies.

In their last phase, very heavy stars can undergo an extreme compression due to gravity. This happens after they have fused all the

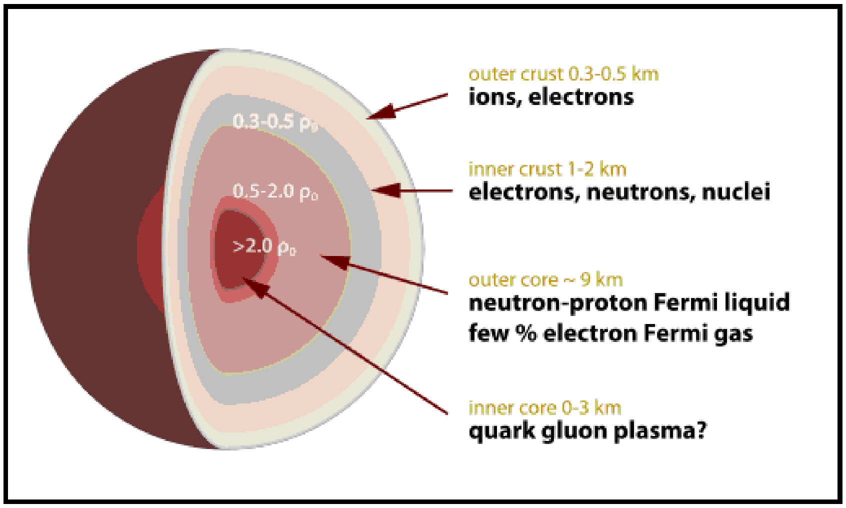

Figure 1.4: Internal structure of a neutron star.

available combustible material and the gravitational pressure is not balanced by the radiation pressure anymore. In this phase electrons are captured by protons in the core of the star, through the inverse β decay. The density in the core of a neutron star is enormous ($\sim 10^{15}$ g/cm^3), which means that the energy density inside a neutron star could be high enough for a QGP to form. In fig. 1.4 the internal structure of a neutron star is pictured.

1.3 First experimental evidences of the QGP

The Quark-Gluon Plasma is an unstable phase of matter, evolving into ordinary hadrons after few tens of fm/c. It is thus impossible to study this phase of the matter directly. Its existence is inferred by the measurement of a number of indirect observables. A variety of experimental signatures has been proposed so far.

1.3.1 Strangeness enhancement

Strangeness enhancement is expected in a QGP medium [4]. Inside the hadrons, the mass of the s quark is estimated to be ~ 50 times larger than the that one of the u and d quarks. However in the hot QGP the SU(3) chiral symmetry between the u, d and s quarks is expected to be restored, which means that their masses all tend to zero; in addition the Pauli principle forbids the formation of additional u and d quark states in the small volume where the QGP is formed. The two effects increase the probability of strange quark pair formation with respect to cold nuclear matter. Therefore in ultra-relativistic heavy-ion collisions, leading to a QGP state, a global enhancement of strangeness production relative to proton-proton and proton-nucleus interactions is expected.

The most interesting result is the multi-strange baryon production at mid-rapidity, first studied by the WA97 [6] and then by the NA57 collaborations [5] at SPS. In fig. 1.5 the strange baryon production (particle/event per partecipant nucleon) in Pb–Pb collisions is plotted as a function of the number of participant nucleons, normalized to the same ratio for pBe. The enhancement factor is apparent and reaches a value of 20 for the Ω (which has a strangeness content $S = 3$). As predicted, the enhancement E increases with the strangeness content: $E(\Lambda) < E(\Sigma) < E(\Omega)$. In particular this behavior cannot be explained by hadronic re-scattering processes where multi-strange baryon and anti-baryon production would be suppressed relative to K and Λ due to their higher threshold. On the contrary, the strangeness increase must have origin at the partonic level, before hadronization.

1.3.2 Quarkonia in the QGP

Bound states of quark-antiquark pairs are known as "quarkonia". The J/Ψ is one of the lowest energy states of a charm-anticharm pair, while the Υ is a bottom-antibottom state.

J/Ψ suppression was expected [7] at SPS energies as a consequence of the screening of the color field in the QGP state, which reduces interactions between a charm-anticharm pair. It was indeed observed by the NA50 experiment [8].

More recently, new theoretical models suggested different mechanisms of quarkonia production in the QGP at the LHC energies. In these models the motion of particles in the QGP is predicted to be analogous to the Brownian motion. A number of dynamic transport models predict that these particles can recombine in the final stages of the QGP evolution, leading to an enhancement of charmonium produc-

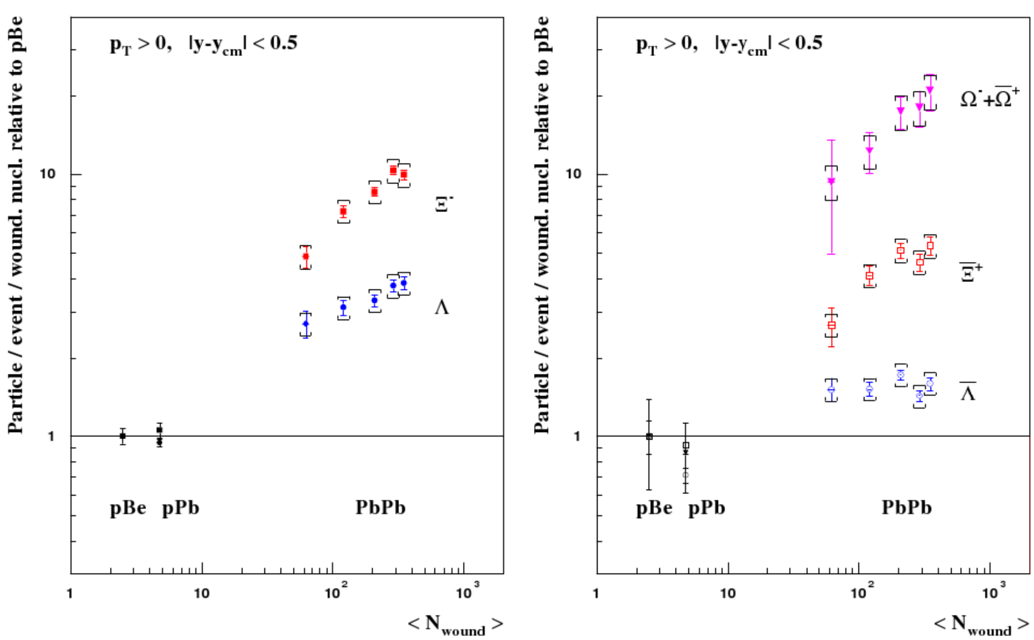

Figure 1.5: Multi-strange hadron yield as a function of the number of participant nucleons, normalized to the ratio pBe, measured by the NA57 experiment at the SPS [5].

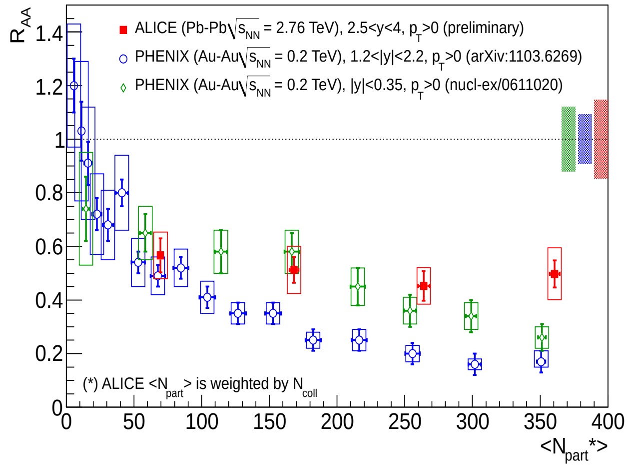

Figure 1.6: J/Ψ R_{AA} measured by ALICE as a function of $\langle N_{part}\rangle$ in Pb–Pb collisions at $\sqrt{s_{\mathrm{NN}}} = 2.76$ TeV compared to PHENIX results in Au-Au collisions at $\sqrt{s_{\mathrm{NN}}} = 200$ GeV [9].

tion, especially at low transverse momentum.

The ALICE collaboration has measured [9] the nuclear modification factor, R_{AA} for the J/Ψ meson in Pb–Pb collisions at $\sqrt{s_{\mathrm{NN}}} = 2.76$ TeV as a function of centrality. This quantity is defined as the ratio between the number of J/Ψ mesons produced in heavy-ion collisions over that produced in proton-proton collisions, scaled accordingly using a Glauber model [10]. An R_{AA} close to unity means that a heavy-ion collision can be treated as a superposition of nucleon-nucleon collisions, without the intervention of any collective effect. The measurements have been done down to very low transverse momentum, where recombination of the charm quarks in the QGP is expected to be the main production mechanism. The ALICE measurement, shown in fig. 1.6, shows that R_{AA} has very little dependence on centrality, and is significantly higher than the previous observations at RHIC.

Recombination makes it difficult to accurately determine the suppression of the J/Ψ so now experiments are looking at the heavier quarks, e.g. bottomium, where recombination effects are expected to be much less. The CMS collaboration has recently reported [11] a measurement about the excited Υ states in Pb–Pb collisions at $\sqrt{s_{\mathrm{NN}}} =$ 2.76 TeV. The Υ has been measured in three of its states, which are known as 1S, 2S and 3S. The 1S is the ground state of the Υ while the others are excited states. Since these are more weakly bound, they are less likely to survive in the QGP matter, and are expected to be more suppressed. Conversely most of the models suggest that the 1S state will survive at LHC collision energies which makes it a good standard to compare to. They measured the double ratio

$$[\Upsilon(2S+3S)/\Upsilon(1S)]_{\mathrm{Pb-Pb}}/[\Upsilon(2S+3S)/\Upsilon(1S)]_{\mathrm{pp}} \tag{1.2}$$

which turned out to be well below unity, with a significance such that the probability of being 1 is less than 1%.

1.4 A new energy regime: RHIC and LHC

The results of the SPS program at CERN, and in particular the enhancement of strangeness production and the J/Ψ suppression together with other evidence coming from different phenomenologies, allowed the conclusion that in Pb–Pb collisions a new state of matter is formed in which the effects of quark confinement appear to be removed. In February 2000 CERN announced officially that from these and other results, evidence for the formation of a new state of matter has emerged [12].

In the meantime the Relativistic Heavy-Ion Collider (RHIC) at BNL was starting operations, colliding copper and gold ions at center of mass energies ranging from 19.6 GeV to 200 GeV per nucleon. In 2009 the Large Hadron Collider (LHC) at CERN began fully operational as well. Pb–Pb collisions have been already collected during 2010 and 2011 at $\sqrt{s_{\mathrm{NN}}} = 2.76$ TeV, and more is expected in the years to come.

The new energy regimes have allowed RHIC and LHC experiments to look at new, yet unexplored observables, opening a new era of measurements in heavy-ion physics.

1.4.1 Jet quenching

In the new energy regimes of RHIC and LHC, the cross section for the production of high p_{T} partons is considerably higher and the so-called hard-processes become experimentally accessible. Such hard probes originate from partonic scatterings with large momentum transfer Q^2 and are directly coupled to the fundamental QCD degrees of freedom. Moreover they are produced in very short time-scales, allowing them to propagate through (and potentially be affected by) the medium.

The effect of the in-medium parton energy loss results in the attenuation or disappearance of the jet arising from the fragmentation of the outgoing parton. The phenomenon described above is known as “jet quenching”. Measurements of jet quenching effects have the potential to probe the medium at the hottest, densest stage of the collision.

In fig. 1.7 a hard collision between two partons with the subsequent production of two back-to-back jets is pictured. The energy and momentum conservation implies that the partons coming out of the hard scattering process are emitted in opposite directions with the same transverse momentum. However while one of the partons goes out directly to the vacuum, the other one goes through the dense plasma created, suffering energy loss due to medium-induced *gluonstrahlung*, before fragmenting outside into a (quenched) jet. The amount of energy radiated by the first parton while traversing the medium is proportional to the density of the medium itself and to the squared path length travelled.

Medium-induced parton energy loss in nucleus-nucleus reactions results in various observables which are modified compared to the same

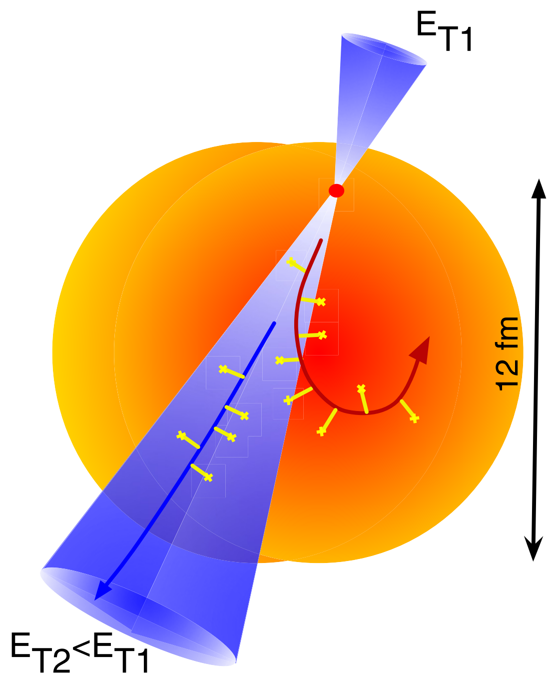

Figure 1.7: Schematic representation of partonic energy loss in the hot and dense medium leading to jet quenching. The parton traveling longer in the medium leads to a wider jet whose particles are softer in energy.

"in-vacuum" measurements in proton-proton (pp) collisions. The presence of jet quenching manifests itself via:

1. Suppression of the inclusive jet yield.

2. Suppression of di-jet and photon-jet correlations.

3. Energy imbalance in di-jets and photon-jet measurements.

Since jet measurements in high-energy heavy-ion collisions must contend with the large background of soft hadrons in the underlying event, jet studies at RHIC and LHC have initially concentrated on high-p_{T} hadrons and their correlations.

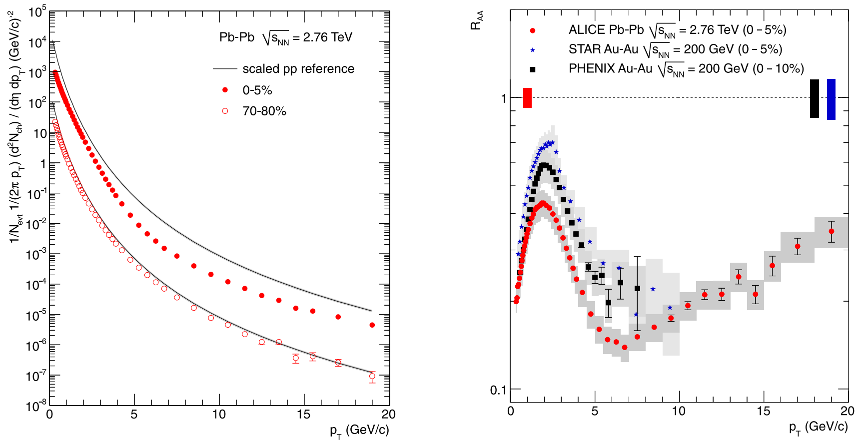

(a) *The* p_{T} *distributions of primary charged particles at mid-rapidity* ($|\eta| < 0.8$).

(b) R_{AA} *in central Pb–Pb collisions at LHC and Au–Au collisions at* $\sqrt{s_{\mathrm{NN}}} = 200$ *GeV by the PHENIX and STAR experiments at RHIC.*

Figure 1.8: Experimental observation of a strong suppression of charged particles at mid-rapidity in central Pb–Pb collisions at $\sqrt{s_{\mathrm{NN}}} = 2.76$ TeV (ALICE [13]).

The simplest empirically testable (and theoretically computable) consequence of jet quenching in heavy-ion collisions is the suppression of the single inclusive high-p_{T} hadron spectrum relative to that in proton-proton collisions. Since most of the energy of the fragmenting parton goes into a single leading hadron, QCD energy loss was predicted to result in a significantly suppressed production of high-p_{T} hadrons. Indeed this has been observed both at RHIC [14, 15] and at LHC [13]. In fig. 1.8a the primary charged particle p_{T} spectra measured by ALICE for central and peripheral Pb–Pb events is compared to a scaled pp measurement. Fig. 1.8b shows the nuclear modification factor R_{AA} of charged particles as measured by ALICE, compared with measurements from PHENIX and STAR.

Jets are produced in pairs in leading order perturbative QCD (pQCD), and high-p_{T} di-hadron correlations in pp collisions should exhibit the

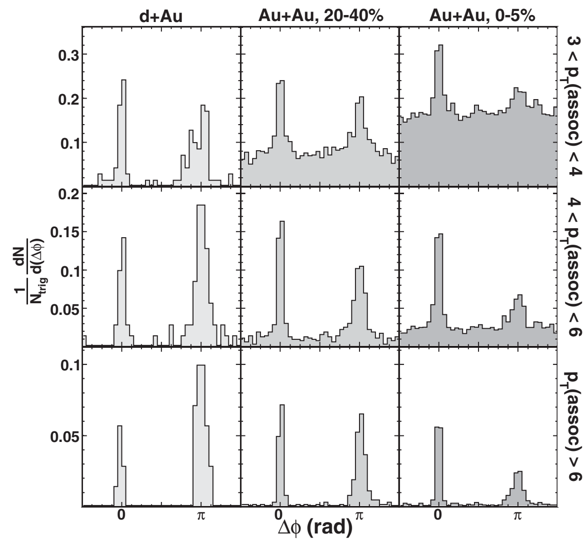

Figure 1.9: Azimuthal correlation histograms of high p_{T} charged hadrons for $8 < p_{\mathrm{T}}^{\mathrm{trig}} < 15$ GeV/c, for dAu, 20%–40% Au–Au, and 0%–5% Au–Au events. $p_{\mathrm{T}}^{\mathrm{assoc}}$ increases from top to bottom [16].

back-to-back jet structure of the underlying hard parton-parton scattering. Jet quenching due to partonic energy loss in nuclear collisions is expected to modify such correlations. Both STAR and PHENIX have performed measurements which confirmed these expectations. Fig. 1.9 shows a STAR measurement of the angular correlation between pairs of high transverse momentum charged particles. The measurement is triggered by an associated particle in a certain p_{T} range. A recoil jet peak is present in deuteron-gold collisions but is strongly suppressed in the central gold-gold data.

These measurements clearly shows that hard processes in heavy-ion collisions cannot be simply explained as a superposition of binary nucleon collisions, but some collective effects must take place in order to explain the observed modification with respect to pp or pA measurements. However the jet physics programs of RHIC and LHC are more ambitious and aim at full jet reconstruction and correlations in order to further understand the mechanisms which are behind the observed modifications.

Chapter 2

The ALICE experiment at the LHC

2.1 The Large Hadron Collider

The first plans about the Large Hadron Collider (LHC) date back in 1984, during a Symposium held in Lausanne, Switzerland. In the following years, the great successes of the Large Electron Positron Collider (LEP) at CERN and the evidences for new physics at the TeV scale from its highly accurate electroweak measurements, made the construction of the LHC a CERN priority. The project was finally approved by the CERN Council in December 1994. The construction had been completed in fall 2008.

The LHC is a two-ring-superconducting-hadron accelerator and collider. It is the most powerful accelerating machine ever built: at its full operation it will accelerate two counter-rotating proton beams up to 7 TeV, and lead beams up to 2.76 TeV. The SPS complex serves as injector for the LHC, providing proton beams at 450 GeV.

The LHC is installed in a 26.7 km underground tunnel, lying between 45 m and 170 m below surface, in the area of Geneva, Switzerland. The tunnel was built at the end of the eighties for the LEP machine,

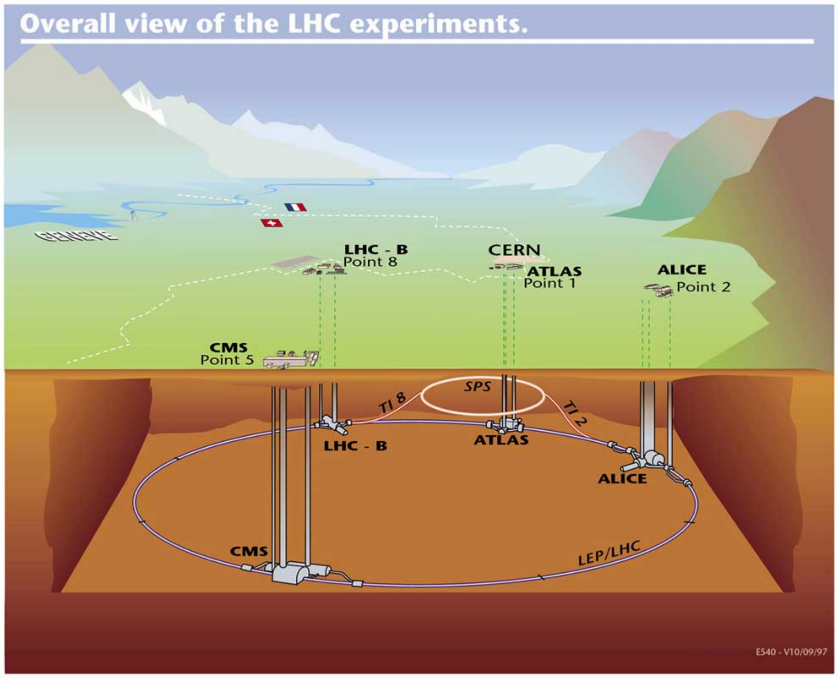

Figure 2.1: The CERN LHC schematic layout and the four principal experiments installed around the ring of the LHC.

which was then dismantled in 2000 to make space for the LHC.

The main technological challenge is represented by the superconducting dipoles, working at a temperature of 1.9 K, which bend the beams around the circumference of the LHC. At 7 TeV these magnets have to produce a field of about 8.4 T.

Luminosity is another challenge which has been embraced by this new machine: the design peak luminosity is $L = 10^{34}$ cm^{2}s^{-1} for proton-proton operation and $L = 10^{27}$ cm^{2}s^{-1} for lead-lead operation. Protons are injected in the storage ring of LHC in bunches, each containing 1.15×10^{11} particles, separated by a 25 ns spacing.

There are four different interaction points, associated to the experiments (ATLAS, CMS, ALICE and LHCb), where the beams collide.

Two smaller experiments TOTEM and LHCf share the interaction point respectively with CMS and ATLAS. A schematic view of the machine is pictured in fig. 2.1.

The first proton beams at the injection energy of 450 GeV circulated in September 2008. Unfortunately a failure in a connection of one of the superconducting magnets caused a one-year stop of the operations. Up to now (November 2012) LHC has collided proton beams at 0.9, 7 and 8 TeV in the center of mass. LHC comes with an ambitious heavy-ion physics program, parallel to the proton-proton physics. Pb–Pb collisions have been already collected during 2010 and 2011 at $\sqrt{s_{\rm NN}} =$ 2.76 TeV, together with a pp run at $\sqrt{s}$ = 2.76 TeV to serve as a baseline. Recently (September 2012) a first proton-lead pilot run at 5.02 TeV in the center of mass has been successfully performed, allowing the experiments to get a first glance at the data [17, 18]. A complete run is scheduled to be collected with a significantly higher statistics in the first weeks of 2013.

After its first "long shut-down", which will take place just after the p–Pb run, LHC will start operating at its full power to collide protons at 14 TeV in the center of mass and lead beams at 5.52 TeV per nucleon.

2.2 ALICE detector overview

ALICE ("A Large Ion Collider Experiment") is the heavy-ion dedicated experiment at the LHC.

The ALICE experiment, as shown in fig. 2.2, consists of a central detector system, covering mid-rapidity ($|\eta| < 0.9$) over the full azimuth, and several forward systems. The central barrel is enclosed by a large solenoidal magnet, which generates a magnetic field up to 0.5 T. The magnet is 12 m long and has a radius of 5 m. The central barrel detectors are listed below, from the innermost to the outermost:

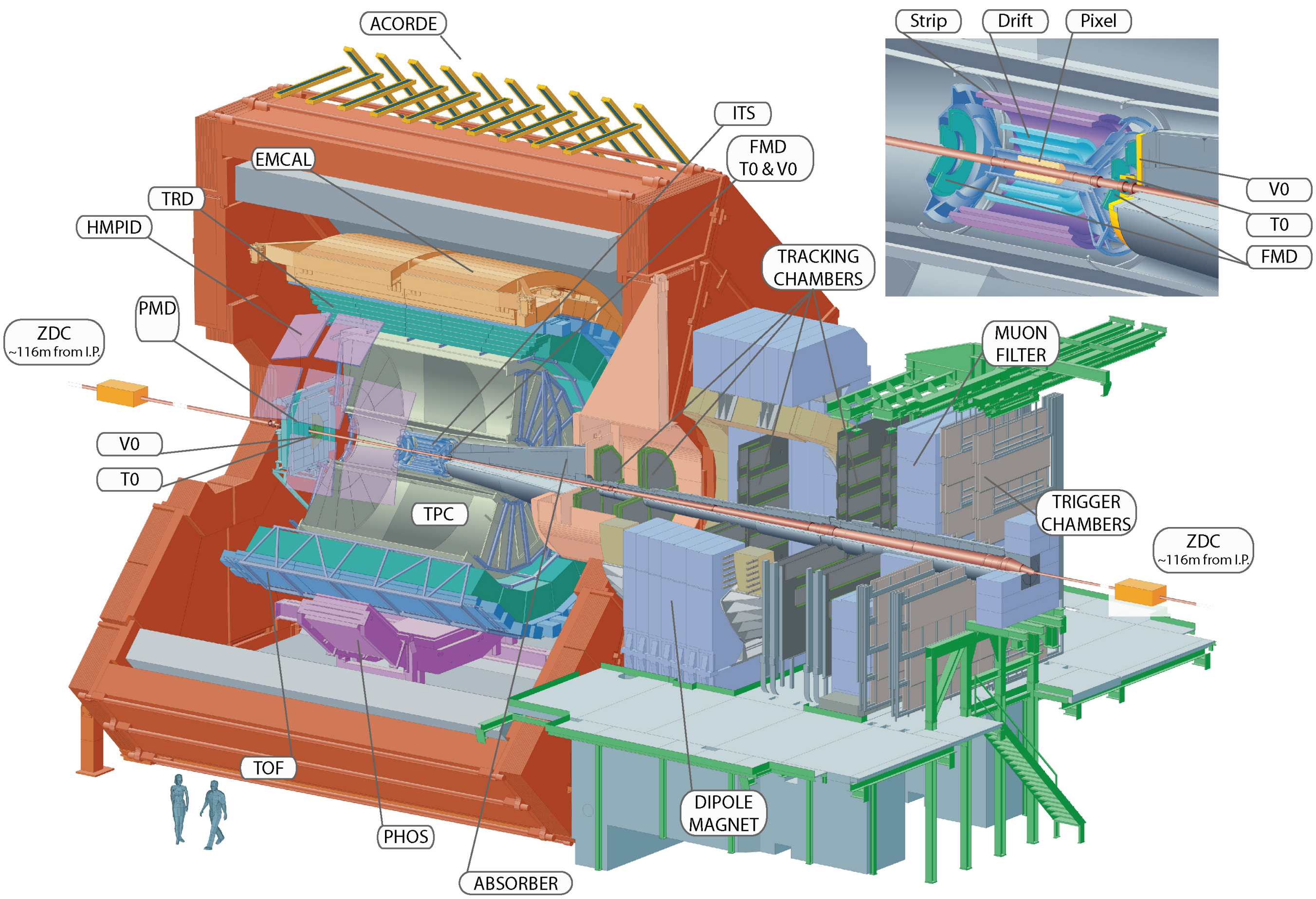

Figure 2.2: ALICE general layout.

– *Inner Tracking System* (ITS), a six-layer silicon detector;

– *Time Projection Chamber* (TPC), the main ALICE tracking detector;

– *Transition Radiation Detector* (TRD), for electron identification;

– *Time-of-Flight* (TOF), for particle identification.

In the outermost layer, but still inside the magnet, there are other detectors with partial azimuthal coverage:

- *Electromagnetic Calorimeter* (EMCal), a sampling Pb-scintillator calorimeter;
- *PHOton Spectrometer* (PHOS), an array of high-density lead tungstate crystals;
- *High-Momentum Particle Identification Detector* (HMPID), an array of ring-imaging Cherenkov detectors.

Finally there is a number of detectors placed in the forward rapidity region:

- *Photon Multiplicity Detector* (PMD), a photon counting detector;
- *Forward Multiplicity Detector* (FMD), a charged particle counting detector;
- T0 and V0, two scintillator and quartz counters to provide fast triggers;
- *Zero-Degree Calorimeter* (ZDC), a hadronic calorimeter;
- *Muon Spectrometer* (MTRK), a gas muon tracking detector, shielded by an absorber.

A summary of the details of detector subsystems and physics performance can be found in Ref. [19]. In what follows I shall briefly describe the ALICE trigger system and the detectors which have been used in the jet reconstruction analysis, namely the ITS, the TPC and the EMCal. For the other subsystems only a brief overview will be given.

2.3 The trigger system

The aim of a trigger system is to select events as efficiently as possible and it plays an especially crucial role in the case of rare events, i.e. those events that do not occur very often in particle collisions.

The ALICE Trigger System is made up of two independent components: a Central Trigger Processor (CTP) and a Trigger Distribution Network. The CTP provides the trigger decision logic, generating triggers for the readout detectors by evaluating inputs from triggering detectors. The Trigger Distribution Network delivers these triggers to the detectors.

The earliest trigger decision (Level 0, or L0) is issued 1.2 μs after the event, L1 is issued at 6.5 μs, and L2 is issued at 88 μs. L1 and L2 decisions provide rejection of L0 triggers.

The High Level Trigger (HLT) is a farm of up to 1000 multiprocessors personal computers which selects and rejects events (in particular pile-up rejection) in order to reduce the event size (region of interest), and also compress the complete event information that is then subject to an on-line analysis.

2.4 The ALICE tracking system

2.4.1 The Inner Tracking System

The ITS is made of six cylindrical layers of high resolution silicon detectors (fig. 2.3). They cover the central rapidity range ($|\eta| < 0.9$). Its main task is to provide the position of the primary vertex and the first points for the tracks.

In table 2.1 the six layers are listed along with their main characteristics. The first two layers make advantage of the Silicon Pixel Detector technologies, with an improved spatial resolution, to improve the vertex

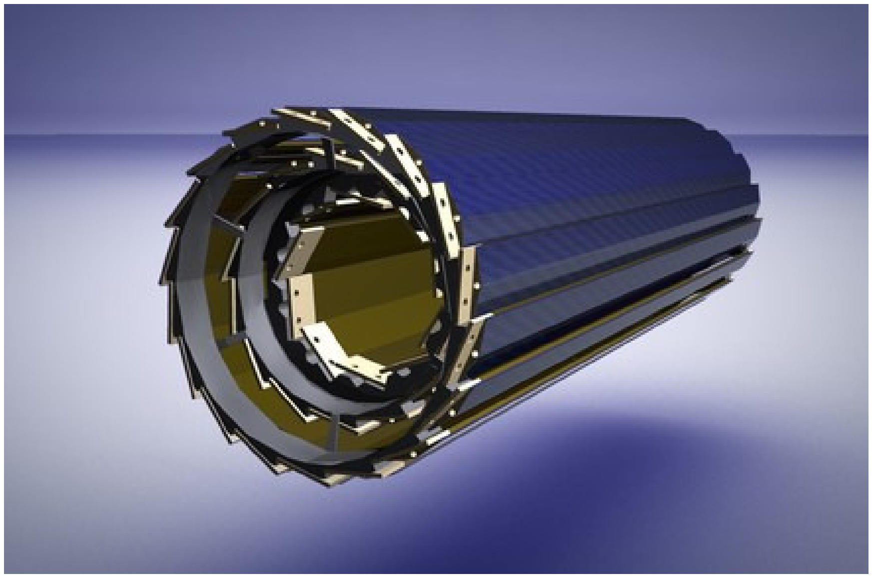

Figure 2.3: Schematic representation of the ITS.

determination.

The momentum resolution for small transverse momentum particles strongly depends on multiple scattering, therefore the amount of materials into the active volume of the ITS has to be at a minimum. For this reason the mechanical frames sustaining the detectors and the associated front-end electronics are made of lightweight carbon-fibres.

2.4.2 The Time Projection Chamber

The TPC is the main tracking detector. It is the biggest Time Projection Chamber ever built. It provides track finding, momentum measurement, particle identification via dE/dx and secondary vertex determination. It is 510 cm long, with an inner radius of 90 cm and an outer radius of 250 cm. The dimension of the TPC ensures a resolution $< 10\%$ in the determination of dE/dx.

The total inner volume (88 m^3) is filled with a mixture 90/10 of Ne/CO_2, which demonstrated good performance.

Table 2.1: Characteristics of the ITS subdetectors.

Layer	Type	r (cm)	$\pm z$ (cm)	Area (m^2)	Tot. channels	Average occupancy (%)
1	pixel	4.0	16.5	0.09	5,242,880	1.5
2		7.0	16.5	0.18	10,485,760	0.4
3	drift	14.9	22.2	0.42	43,008	2.5
4		23.8	29.7	0.89	90,112	1.0
5	strip	39.1	45.1	2.28	1,201,152	4
6		43.6	50.8	2.88	1,517,568	3.3

A nominal negative voltage of 100 KV is applied to the central membrane, creating an electric field of 400 V/cm parallel to the beam line directed towards the membrane, giving an electron drift velocity of 2.8 cm/μs. Each end-cap contains 72 readout pads, arranged into two crowns each of 18 sectors, and a total of 5.7×10^5 channels are present. The pad size (7×4.5 mm^2) is a compromise between the required granularity and costs. A metallic gating grid is positioned at a distance of 3 mm from the cathode wires.

The TPC field cage provides stability and extremely precise positioning of the readout pads and of the central electrode, while maintaining the materials at minimum in order to avoid scattering or absorption of the particles produced in the collision when crossing over the TPC volume. The x, y coordinates of each point are indeed given by the positioning of the readout pads, while the z coordinate comes from the time which the drift electrons take to reach them.

The ITS+TPC combined tracking efficiency is about 85%. In the determination of the transverse momentum the ITS plays an essential role: for tracks which have at least one hit in the ITS the momentum resolution can be as low as a few percent.

2.5 The ALICE Electromagnetic Calorimeter

2.5.1 Overview

The ALICE Electromagnetic Calorimeter [20] was not present in the first design of the experiment. The EMCal project had been approved in October 2006 to become an integral part of the ALICE research program. It provides a fast and efficient trigger for jets, photons and electrons, allowing ALICE to fully exploit the hard momentum processes which are abundantly produced at LHC.

The current layout of the EMCal, sketched in fig. 2.4, consists of 10 full size and 2 "one-third-size" Super Modules (SM). During the first LHC long shut-down, an additional 6 Super Modules, belonging to the DCal (Dj-jet Calorimeter) project [21], will be installed opposite the EMCal, allowing jet-jet, hadron-jet and, possibly, photon-jet correlations.

The EMCal occupies a cylindrical integration volume approximately 110 cm deep in the radial direction, with front face 450 cm from the beam line. The azimuthal EMCal coverage is 107 degrees. In the longitudinal direction the EMCal has a length ~ 700 cm, covering $|\eta| < 0.7$.

The full size Super Modules span $\Delta\eta = 0.7$ and $\Delta\phi = 20°$, whereas the 1/3 modules span a smaller azimuthal range of $\Delta\phi = 7°$.

Each full-sized Super Module is assembled from $12 \times 24 = 288$ modules arranged in 24 strip modules of 12×1 modules each. Each one-third size Super Module is assembled from $4 \times 24 = 96$ modules. Each module comprises four independent energy-measuring channels called "towers". A total of 1,152 towers are in each full size Super Module and 384 in the one-third-size ones, for a total of 12,288 towers.

The total thickness of the calorimeter correspond to 20 radiation

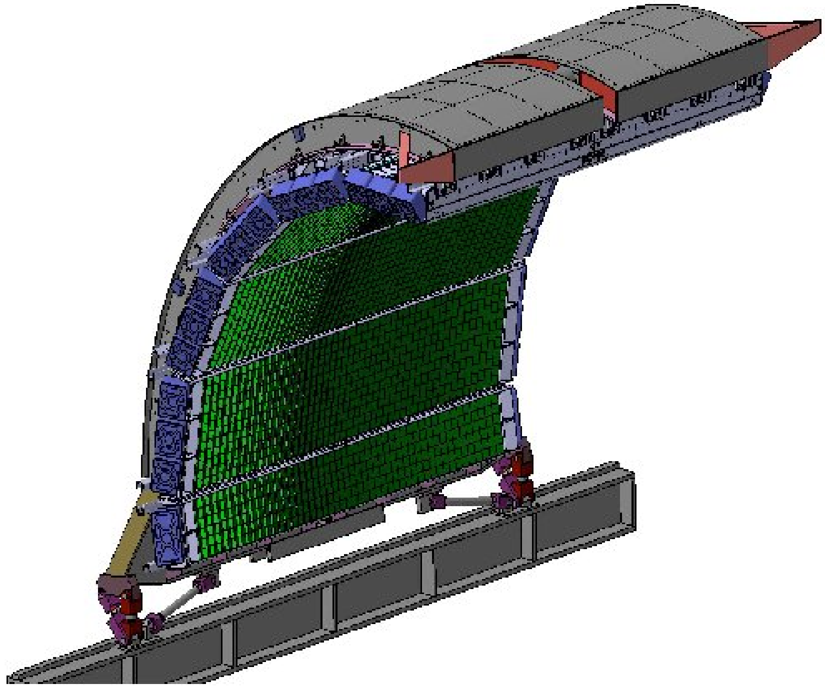

Figure 2.4: A perspective view of the EMCal in its dedicated support structure is shown. Individual super modules are illustrated with front-end electronics crates mounted on the ends, just beyond the support structure.

lengths and it incorporates on average a moderate active volume density of 5.68g/cm^2 which results from a $\sim 1 : 1.22$ Pb to scintillator ratio by volume. The physical characteristics of the EMCal are summarized in table 2.2. An exploded view drawing of the module showing all single components is shown in fig. 2.5

2.5.2 The read-out system

The scintillation light produced in each tower is collected by an array of wavelength shifting (WLS) fibres which run longitudinally through the tower and transmit the light to a 5×5 mm^2 active area Avalanche

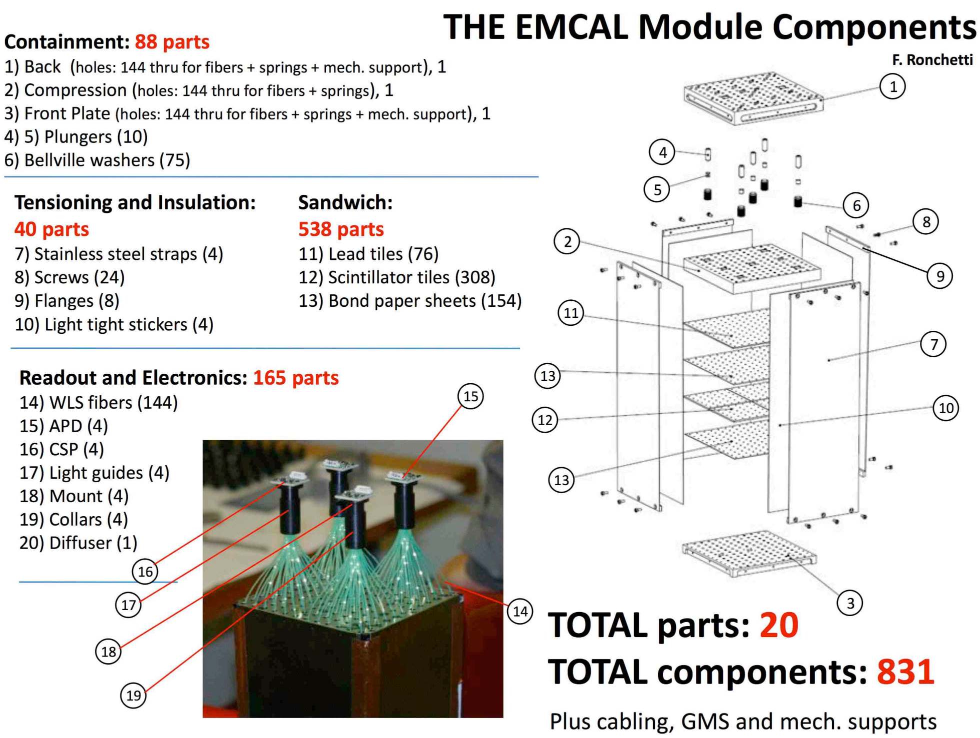

Figure 2.5: Exploded view drawing of EMCal module showing all components.

PhotoDiode (APD). The APDs are operated at moderate gain for low noise and high gain stability in order to maximize the energy resolution. With a nominal APD gain of $M = 30$, about 132 electrons are generated in the APD per MeV of energy deposited by showering electromagnetic particles.

The APD is connected directly to the back of a Charge Sensitive Preamplifier (CSP) which integrates the charge output from the APD over a 1 pF capacitor into a voltage step pulse. The Front End Electronics (FEE) board contains 32 remotely controlled precision High Voltage (HV) bias regulators, 64 shapers and digitizers, a board controller, and

Table 2.2: The EMCal Physical Parameters.

Quantity	Value
Tower Size (at $\eta = 0$)	$\sim 6.0\times \sim 6.0 \times 24.6$ cm (active)
Tower Size	$\Delta\phi \times \Delta\eta = 0.0143 \times 0.0143$
Sampling Ratio	1.44 mm Pb / 1.76 mm Scintillator
Number of Layers	77
Effective Radiation Length X_0	12.3 mm
Effective Moliere Radius R_M	3.20 cm
Effective Density	5.68 g/cm^2
Number of Radiation Lengths	20.1
Number of Towers	12,288
Number of Modules	3072
Number of Super Modules	10 full size, 2 one-third size
Weight of Super Module	~ 7.7 metric tons (full size)
Total Coverage	$\Delta\phi = 107°, \vert\eta\vert < 0.7$

a power regulation system which prevents noise coupling between digital or high Voltage sections and the analog signal section. Four ALTRO chips are required, each containing 16 10-bit flash ADCs and internal multi-event buffers, for a total of 32 high gain and 32 low gain channels per FEE card. The ALTRO ADCs sample the output signals from the shapers at 10 MHz (programmable up to 20 MHz).

2.5.3 Trigger

While offline it is possible to handle the energy deposit corresponding to a single tower, at trigger decision level (L0/L1) the smallest unit is a FastOR, namely an analog summed 2×2 patch of towers. FastOR signals are generated by the FEE cards and sent to the corresponding Trigger Region Unit (TRU) card. The TRU digitizes the sums using a commercial FADC and inputs the full space and time image of all channels to a single FPGA. The L0 trigger runs at this level, where

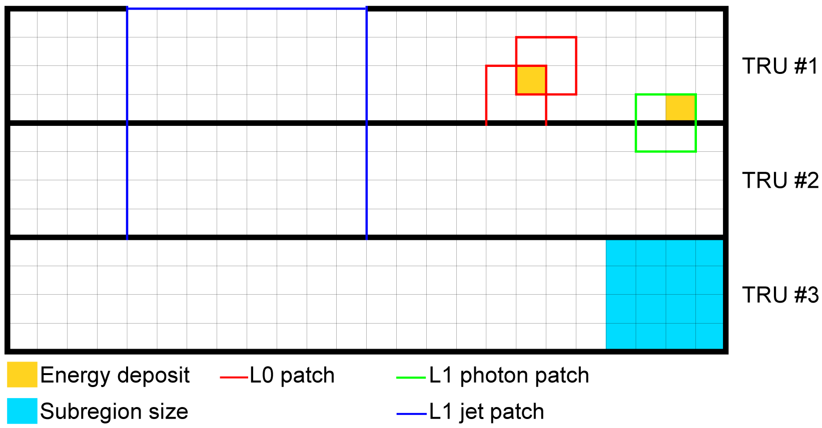

Figure 2.6: A Super Module of the EMCal is sketched. The thick lines represents different TRU. A 2×2 FastORs L0 patch can slide only within TRU, whereas a L1 patch (jet or gamma) can make a patch out of FastORs belonging to different TRU.

decisions can only be based on the local region of the EMCal accessed by a single TRU. In particular the L0 trigger simply applies a threshold to a 2×2 FastORs patch.

Valid L0 triggers (yes/no signals) are sent to Summary Trigger Unit (STU). STU computes the OR of the signals coming from all the 30 TRUs to make the trigger decision. Upon L0 trigger accepted from ALICE CTP (Central Trigger Processor), complete FastOR data is delivered to STU. The STU inputs them to a single FPGA. At this point L1 trigger algorithms can take decisions based on the information coming from all the TRUs. This is particularly useful as QCD jets subtend an area larger than that accessed by a single TRU. The jet patch trigger in the STU employs a simple jet-finding algorithm applied over the EMCal acceptance, in which the energy is integrated within a patch of defined size and the patch is stepped over the entire EMCal fiducial area. A L1 jet trigger signal is issued if a patch energy in the event exceeds a defined threshold.

2.6 The other subsystems

2.6.1 The V0 detector

The V0 is a small angle detector located on either sides of the ALICE interaction point. It consists of 2 discs of segmented (8 segments) plastic scintillator tiles read out by optical fibers. The two discs are known as V0A, which covers $-3.4 < \eta < -1.7$, and V0C, which covers $1.7 < \eta < 5.0$. By requiring the coincidence from both sides, the beam-gas interactions are efficiently rejected.

The V0 detector serves as main trigger for "minimum bias" pp events and for centrality selected Pb–Pb events, in which case higher thresholds are applied.

The V0 detector information is also used to characterize Pb–Pb events, determining centrality and event plane.

2.6.2 The Time of Flight Detector

The ALICE Time of Flight Detector provides particle identification capabilities in the intermediate momentum range $0.5 < p_{\mathrm{T}} < 2.5$ GeV/c. The TOF detector measures the transit time of individual particles coming from the TPC with a very good time resolution (120 ps). This goal has been achieved making use of the technology of the Multi-gap Resistive Plate Chambers (MRPC).

2.6.3 The Transition Radiation Detector

The main goal of the ALICE Transition-Radiation Detector (TRD) is to provide electron identification in the central barrel for momenta greater than 1 GeV/c, where the pion rejection capability through energy loss measurements in the TPC is no longer sufficient. The TRD consists of six layers of radiator foil stacks followed by Time Expansion Chambers filled with Xe/CO_2, providing an e/π rejection power of 100 in high multiplicity operation.

2.6.4 The High Momentum Particle Identification Detector

The High-Momentum Particle Identification Detector (HMPID), is dedicated to inclusive measurements of identified hadrons for $p_{\mathrm{T}} > 1$ GeV/c. It was optimized to extend the useful range for π/K and K/p discrimination, on a track-by-track basis, up to 3 and 5 GeV/c respectively. The HMPID is based on on proximity-focusing Ring Imaging Cherenkov (RICH) counters, placed at a distance of ~ 4.5 m from the beam axis.

2.6.5 The PHOton Spectrometer

The PHOton Spectrometer (PHOS) was designed to detect electromagnetic particles with high efficiency for photon identification and neutral mesons reconstruction via their decay channel to photons from low to moderate transverse momentum. The PHOS is located 5 m vertically beneath the interaction region and its coverage is $|\eta| > 0.12$ in pseudorapidity and $\Delta\phi = 100°$ in azimuthal angle. The detector is built from 256 $PbWO_4$ crystals, a material with small Moliere radius and high light output. Avalanche PhotoDiodes (APDs) are used as photodetectors. The electronics provide both energy and time information to reject neutrons and a trigger for high-p_{T} photons.

2.6.6 The other forward detectors

The Forward Multiplicity Detector

The main functionality of the silicon strip Forward Multiplicity Detector (FMD) is to provide (offline) charged-particle multiplicity information. The FMD consists of a mosaic of silicon pad channels distributed over five ring counters, two on the muon arm side, where space is more limited, and three on the opposite side.

The Photon Multiplicity Detector

The Photon Multiplicity Detector (PMD) measures the multiplicity and spatial distribution of photons on an event-by-event basis in the forward region of ALICE. The PMD consists of two identical planes of detectors with a $3X_0$ thick lead converter in between them.

The T0 Counters

The T0 counters are 24 Cherenkov radiators which provides the event time with a precision of less than 50 ps.

The Zero Degree Calorimeters

The four small and very dense Zero Degree Calorimeters (ZDC) can be used to measure and trigger on the impact parameter of the collisions, looking at the nucleons which did not take part in the collision (spectators).

The Forward Muon Spectrometer

In heavy-ion operation, the Muon Spectrometer can identify muons with momentum above 4 GeV/c allowing the study of vector meson resonances via their $\mu^+\mu^-$ decay. The spectrometer consists of a front absorber placed 90 cm from the interaction point, a 15 m long small angle absorber, a large dipole magnet with a 3 Tm integrated field, 10 high-granularity tracking chambers, a muon filter made of a 1.2 m thick iron wall and four large area trigger chambers.

Chapter 3

Jet physics with the ALICE experiment

3.1 Jet physics in heavy-ion collisions: state of the art

Recently many studies aiming at full jet reconstruction in heavy-ion environment have been pursued both by RHIC and LHC experiments. The field has been greatly enriched by these studies and much progress has been made.

At the Quark Matter 2009 Conference, STAR presented [22] a first attempt at full jet reconstruction in Au–Au collisions at $\sqrt{s_{\rm NN}} = 200$ GeV. The measurement makes use of the Anti-$k_{\rm T}$ and $k_{\rm T}$ algorithms, which will be presented below. Some additional progress in dealing with background fluctuations in the heavy-ion environment was presented by STAR at the Hard Probes 2010 Conference [23]. Some of the ideas presented there, in particular the event-by-event background subtraction and the successive deconvolution of background fluctuations, have been employed in this analysis.

Very recently some interesting results have been published by LHC experiments. In 2010 ATLAS reported a measurement [24] on the obser-

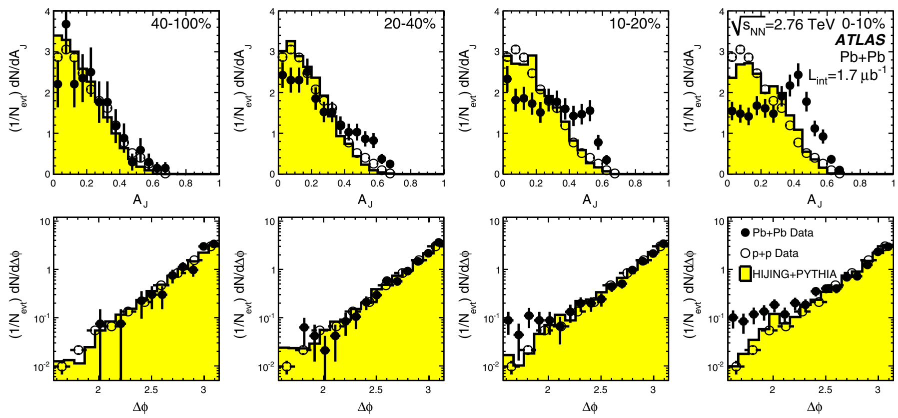

Figure 3.1: (Top) Di-jet asymmetry distributions for data (points) and unquenched HIJING (solid yellow histograms), as a function of collision centrality. Proton-proton data are shown as open circles. (Bottom) Distribution of $\Delta\phi$ the azimuthal angle between the two jets. [24]

vation of a centrality-dependent di-jet asymmetry in Pb–Pb collisions at $\sqrt{s_{\mathrm{NN}}} = 2.76$ TeV. To measure the asymmetry they looked at the distribution of the ratio:

$$A_J = \frac{E_{T1} - E_{T2}}{E_{T1} + E_{T2}}, \tag{3.1}$$

where E_{Ti} is the reconstructed transverse energy of the jet using calorimeter detectors. The measurement is simplified by the fact that they only triggered on jets with $E_{\mathrm{T}} > 100$ GeV/c, thus removing any combinatorial background. Nevertheless the result (fig. 3.1) is very interesting as a clear asymmetry is observed in central Pb–Pb collisions, indicating that some processes leading to jet suppression have occurred. A similar measurement has been reported by the CMS Collaboration using similar cuts on the selected jets [25].

ALICE has published a paper about a background fluctuation measurement for jet analysis [26]. Some preliminary results on jet reconstruction in Pb–Pb collisions using only charged constituents have been presented [27] at conferences as well.

In what follows the first full jet reconstruction in Pb–Pb collisions at $\sqrt{s_{\rm NN}} = 2.76$ GeV/c using the ALICE detector will be presented. In particular the next paragraphs will be devoted to a detailed description of the analysis procedures. Results will be shown in the next Chapter.

3.2 Event selection

The analysis makes use of the Pb–Pb events at $\sqrt{s_{\rm NN}} = 2.76$ GeV/c recorded by the ALICE experiment in fall 2011. Sixty-four runs of data taking have been analyzed corresponding to about 19.7 millions "minimum bias" events, triggered by the V0 detector. In offline analysis the V0 triggered events can be selected using three different trigger classes, which are coded as follows:

- `kCentral`, 0-10% centrality range;
- `kSemiCentral`, 10-50% centrality range;
- `kMB`, 0-90% centrality range.

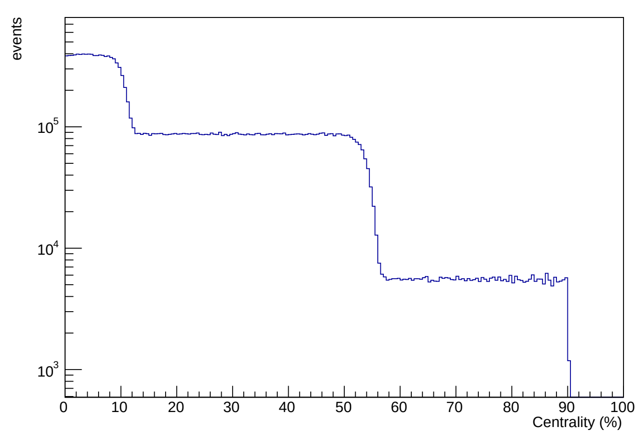

Figure 3.2: Event centrality distribution obtained selecting `kCentral + kSemiCentral + kMB`.

Table 3.1: The four centrality ranges used for the analysis. Events A belong to the "good" event category, where all the TPC sectors were active; events B belong to the "semi-good" category, where the TPC IROC-13 sector was switched off.

Centrality	Events A (millions)	Events B (millions)	Events A+B (millions)
0-10%	3.7	5.6	9.3
10-30%	1.8	3.0	4.8
30-50%	1.7	2.6	4.3
50-90%	0.6	0.7	1.3
Total	7.8	11.9	19.7

Fig. 3.2 shows the event centrality distribution obtained using the combination of the three trigger classes listed above.

The sixty-four runs are divided further into two categories: "good" (A) runs and "semi-good" (B) runs, depending on the operational condition of the TPC. Group A runs were taken with a fully operational TPC while in group B the IROC-13 sector was switched off, which resulted in a region of the (η, ϕ) plane with very limited tracking efficiency. Since this region of limited tracking efficiency is not within the EMCal acceptance, these runs can be used for analyses that focus on the EMCal (see fig. 3.5).

The whole analysis is done for the four different centrality ranges in table 3.1, focusing particularly on the most central events.

Other event quality cuts have been employed, in order to assure a clean data sample. In particular events are rejected when the primary vertex is far from the center of the detector: $vertex_z < 10$ cm.

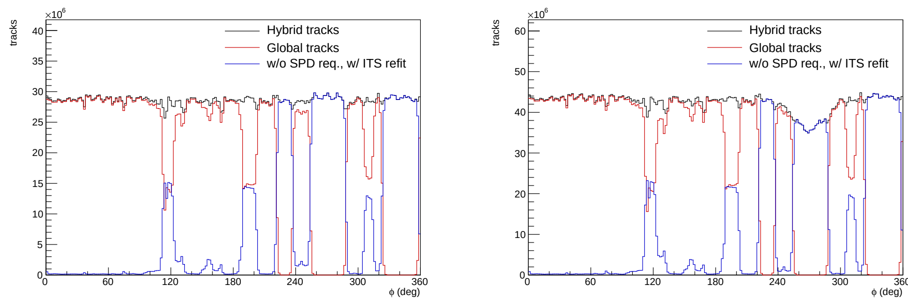

(a) *Group A events ("good").*　(b) *Group B events ("semi-good").*

Figure 3.3: Track azimuthal distributions.

3.3 Track and cluster selection

Jets in ALICE are reconstructed using charged tracks from the tracking system and clusters from the electromagnetic calorimeter. In par. 3.3.1 the track quality cuts will be outlined. Some corrections have to be done to the clusters in order to avoid energy double counting by including energy in the EMCal left by charged particles. Indeed charged particles always release some of their energy in the calorimeter, but they are already taken into account from tracking. This correction procedure is described in par. 3.3.2.

3.3.1 TPC and ITS track quality cuts

Jet analyses require ambitious track quality cuts, especially to ensure homogeneous tracking efficiency within the acceptance. Non-homogenities may result in artificial correlations. Also background studies are affected because any non-homogeneous inefficiency results in additional region-to-region fluctuations.

The common track reconstruction procedure in the central barrel of the ALICE detector is mainly based on clusters in the Time Projection Chamber (TPC) and on the Inner Tracking System (ITS). Hits in the

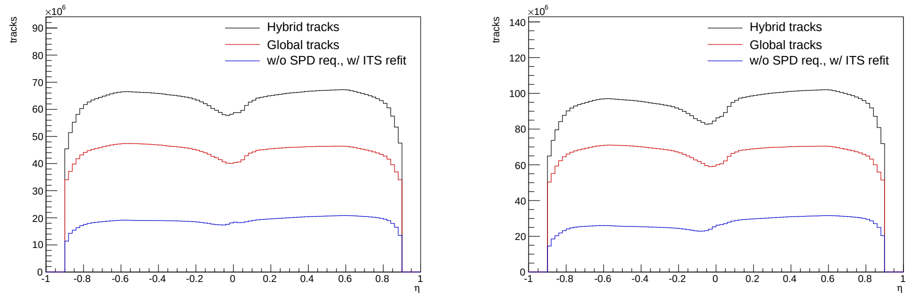

(a) *Group A events ("good").* (b) *Group B events ("semi-good").*

Figure 3.4: Track pseudorapidity distributions.

two innermost layers close to the vertex, namely the Silicon Pixel Detector (SPD), are important for good momentum resolution, because they provide a stronger constrain on the calculation of the magnetic field bending. Since some parts of the SPD were switched off during the considered data taking period, inefficient regions for global track reconstruction, i.e. tracks which contains both ITS and TPC points, are apparent. To ensure a flat distribution in the (η, ϕ) plane, a "hybrid" track approach is used:

1. global tracks with SPD hit(s) and an ITS refit;

2. global tracks without SPD hit and with an ITS refit, constrained to the primary vertex.

When available, tracks of the first type with ITS information are used. Those tracks have the best resolution in transverse momentum p_{T}. In the regions where this type of track is not available, tracks of the second type are accepted. They are constrained to the primary vertex to improve their momentum resolution in spite of the missing hit in the SPD. Fig. 3.3 shows the azimuthal distribution of the two track types which make the hybrid tracks used in the analysis. The pseudo-rapidity distributions are shown in fig. 3.4. The distributions are shown sepa-

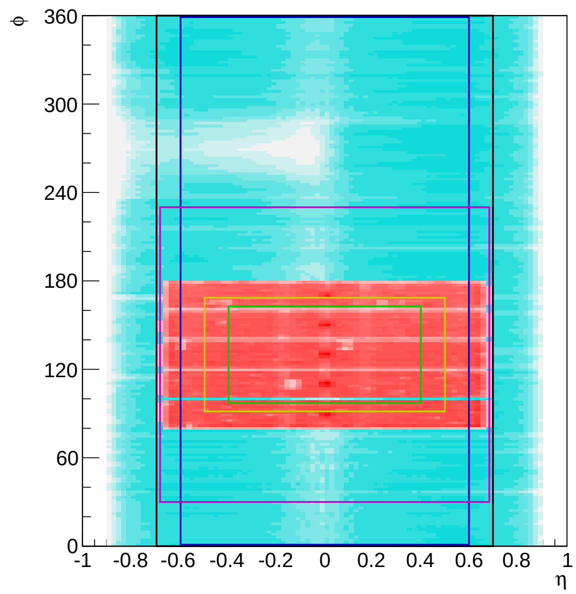

Figure 3.5: Inclusive η, ϕ map of reconstructed charged tracks (light blue) and EMCal clusters (red). The black line represents the fiducial TPC acceptance for a jet cone radius R=0.2, i.e. the region where the jet axis must be accepted; TPC fiducial region for R=0.3 is represented with the dark blue line, the EMCal fiducial region for R=0.2 with the yellow line and R=0.3 with the green line; the region used to estimate the background is shown in magenta.

rately for group A and group B. As expected the hybrid track azimuthal distribution is flat in the first case, while in the latter case there is a dip at $\sim 275^{\circ}$, corresponding to the inactive TPC sector. Fig. 3.5 shows a map of reconstructed tracks and EMCal clusters, where the dip in the TPC efficiency is apparent. The fiducial acceptances for different jet reconstruction parameters are also shown.

3.3.2 EMCal cluster selection and corrections

The jet energy carried by electromagnetic radiation is measured by the EMCal. The clusterizing algorithm "v2", which is the standard choice for Pb–Pb data, is employed in this analysis. The basic idea of this algorithm is to aggregate cells to the cluster until reaching a cell with more energy than the precedent. This algorithm insures that there is only a single local maximum in each cluster. The "3×3" clusterizer algorithm has been also proposed for Pb–Pb events. It creates clusters around a local maximum cell. The maximum dimension of the cluster is limited to a square with 3 cells in each sides.

It is worth noting that since jet reconstruction is based on energy flow, accurate reconstruction of π^0 and other neutral particles is not required, as long as all EM energy is accounted for. The only requirement for the clusterizer algorithm is that it should not make too large clusters in order to avoid interferences with the jet finder.

Before clusterization a zero suppression cut on the cell energy is applied, requiring $E_{\mathrm{cell}} > 50$ MeV.

In what follows, some aspects of the EMCal calibration will be presented. Standard calibration of the EMCal (done at reconstruction level) includes energy calibration, which is done through the measurement of the π^0 mass peak, and tower alignment.

Fig. 3.6 shows the map of the inactive, bad and warm towers in the EMCal acceptance. Candidate bad towers are first identified automatically using a set of well-defined criteria, e.g. criteria which look at the frequency of tower being over threshold with respect to the average. A tower is marked warm if its behavior is ambiguous, e.g. it acts as bad only in certain runs. In this analysis warm towers have been treated as bad towers, i.e. they have been excluded.

Additional recalibrations are done at analysis level.

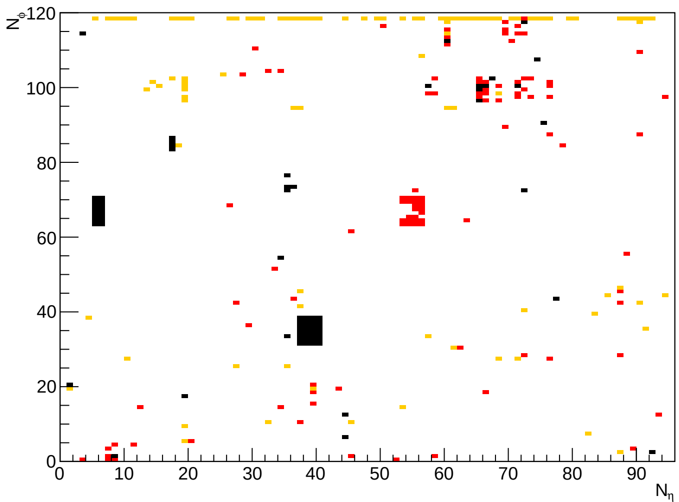

Figure 3.6: Bad channel map: inactive towers (black), hot towers (red), "warm" towers (orange).

Non-linearity correction The calorimeter response to EM radiation is not completely flat as a function of incident energy. In fact the response to low energy particles is reduced by recombination effects while very high energy particles (> 100 GeV/c) may result in a partially contained shower. This correction is estimated through electron beam tests which have been performed during the commissioning of the detector. The non-linearity function used to correct data is shown in fig. 3.7.

Temperature dependent correction The calorimeter response depends to some extent on the operational temperature, due to the variation in the APD gain. This information is recorded during data taking to allow a more accurate energy recalibration during offline analysis.

"Exotic" clusters removal Some "exotic" clusters have been iden-

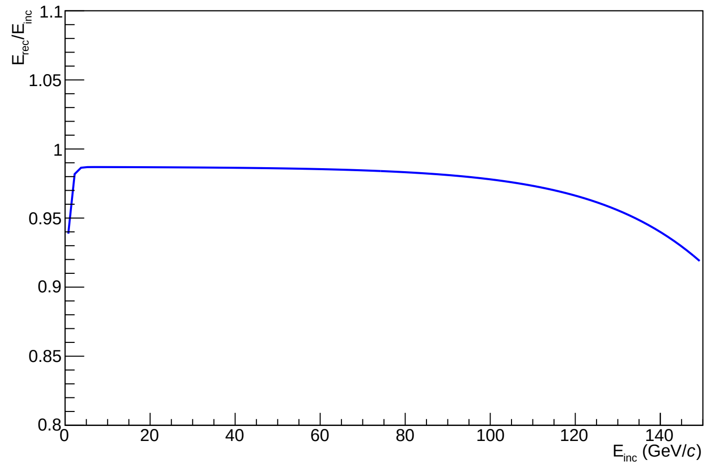

Figure 3.7: Non-linearity function used to correct the cluster reconstructed energy.

tified. Their characteristic is to contain a very high energy tower, almost isolated (i.e. with very few neighbor towers above threshold). These clusters are not easily reproduced in *Monte Carlo* simulations and are believed to come from slow neutrons interacting directly with the APDs. The rejection criterion of such exotic clusters is based on the value for each cluster of the quantity

$$F_{\text{cross}} = 1 - \frac{E_{\text{cross}}}{E_{\text{seed}}} \tag{3.2}$$

where E_{seed} is the energy of the most energetic tower in a cluster and E_{cross} is the sum of the energies of the three or four towers in the cluster that share an edge with it. Fig. 3.8a shows the distribution of F_{cross} as a function of cluster energy E. It can be seen that a large fraction of the energetic clusters have a value of F_{cross} close to unity. Fig. 3.8a shows the cut to exclude such clusters. The inset of fig. 3.8a shows the projected distribution of F_{cross}. The blue vertical line indicates the rejection cut, with accepted

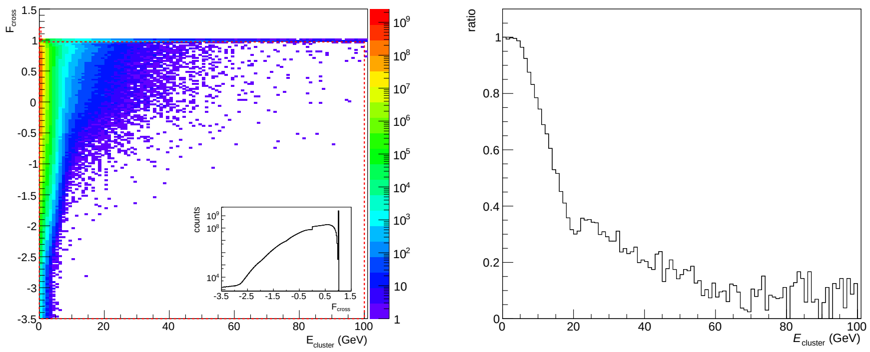

(a) $F_{\rm cross}$ *as a function of the cluster energy* $E_{\rm cluster}$. *In the inset: the projected distribution of* $F_{\rm cross}$.

(b) *Rejection rate.*

Figure 3.8: "Exotic" cluster cut.

clusters having $F_{\rm cross} < 0.97$. Fig. 3.8b shows the rejection rate, which increases with increasing cluster energy. For clusters with $E > 50$ GeV, about 90% are rejected as background by this cut.

3.3.3 Charged energy double-counting

Electrons and positrons induce full EM showers in the EMCal. While charged hadrons most often generate MIP ("Minimum Ionizing Particle") energy deposition in the EMCal, they can also generate partially-contained hadronic showers. However, charged particles are also measured by the tracking system, so correction to the EMCal clusters for showers due to charged particles must be applied to avoid double-counting of this component of the jet energy.

Cluster-Track matching

In order to subtract the charged particle energy from the associated clusters, measured charged track trajectories are propagated to the EMCal surface. Track trajectories are extrapolated in small steps, taking

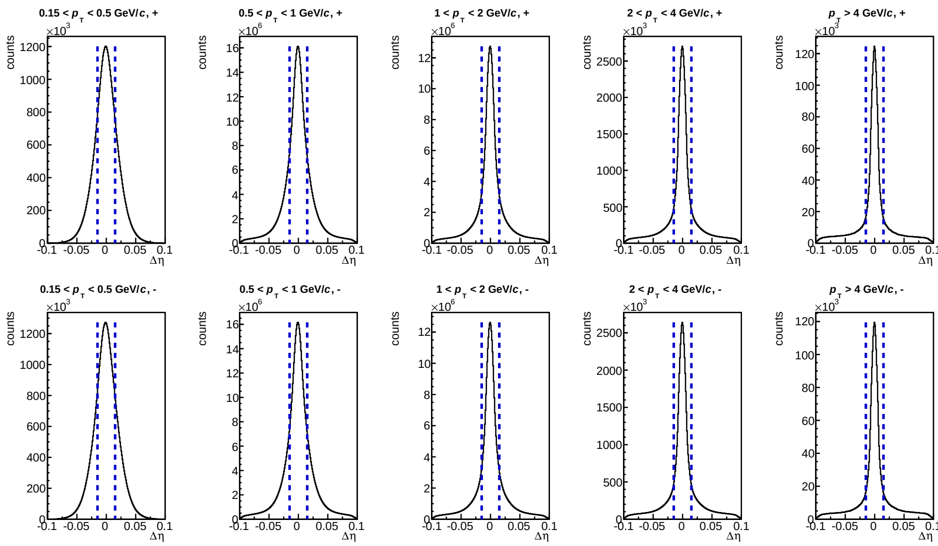

Figure 3.9: Track-cluster matching $\Delta\eta$ distributions for 0-10% Pb-Pb events. The top row is for positive charged tracks and the bottom are negative tracks. The momentum of the tracks increases from left to right.

into account the bending due to the magnetic field, and corrected for energy loss in the intervening material. Fig.3.9 and 3.10 show the residual distributions for matched track-cluster pairs. The widths of the distributions are 0.020 in η and 0.023 in ϕ. Each propagated trajectory is matched to its closest EMCal cluster, with the matching requirement $|\Delta\eta| < 0.015$ and $|\Delta\phi| < 0.03$, as illustrated by the blue vertical lines in fig. 3.9 and 3.10. Multiple tracks can be matched to the same cluster, however each track is required to match at most one cluster. If there are multiple candidate clusters for a single track, the nearest one is chosen. The probability that a cluster has multiple tracks matched to it increases with centrality. The number of matched tracks versus centrality is plotted in fig. 3.11.

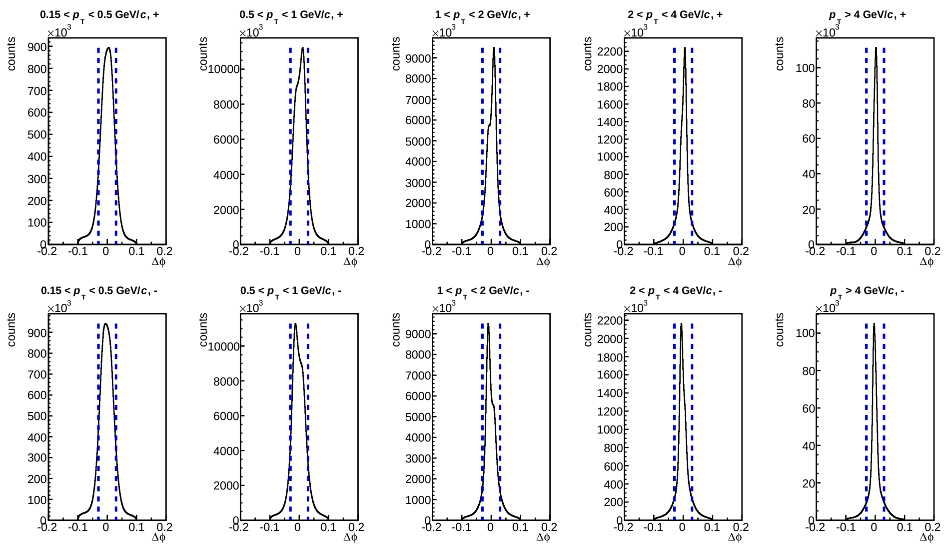

Figure 3.10: Track-cluster matching $\Delta\phi$ distributions for 0-10% Pb-Pb events. The top row is for positive charged tracks and the bottom are negative tracks. The momentum of the tracks increases from left to right.

Correction procedure

Except at very high p_{T}, EM showers due to electrons and positron are well-contained in the EMCal, which therefore measures their full energy with good resolution. However, hadronic showers induced by charged hadrons are only partially contained within the EMCal, and the response to charged hadrons is broader. Fig. 3.12 shows a detector-level simulation of E/p, the ratio of energy to momentum of charged pions with various momenta. Clear minimum ionizing (MIP) peaks are observed at high momentum. At low momentum (upper left) the MIP peak is dominated by a larger component due partially to hadronic showering and partially to the larger thickness of the EMCal for tracks with non-normal incidence.

Correction of cluster energy for charged energy double counting is

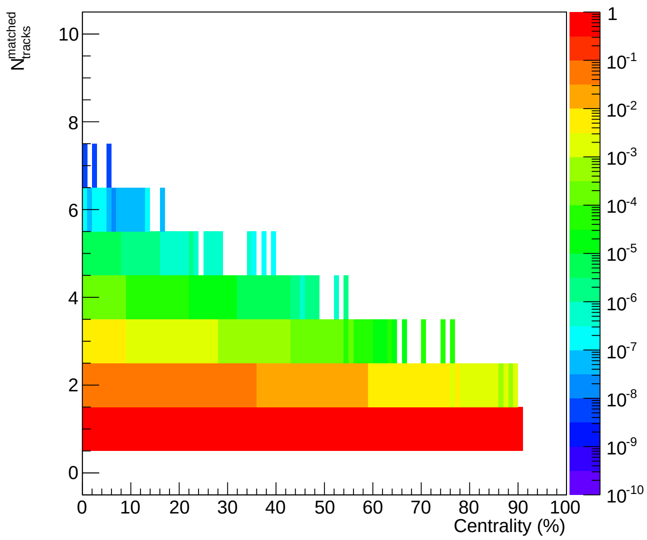

Figure 3.11: Number of matched tracks per cluster as a function of centrality. The z axis (colors) is the probability. Even in the most central events the probability that there is more than one match is $< 5\%$.

based on the following quantity, which is calculated for each cluster having at least one matched track:

$$E_{\mathrm{T,cluster}}^{\mathrm{subtracted}} = E_{\mathrm{T,cluster}}^{\mathrm{reconstructed}} - f \times \sum(p_{\mathrm{T,track}}^{\mathrm{matched}}), \tag{3.3}$$

where $E_{\mathrm{T,cluster}}^{\mathrm{reconstructed}}$ is the cluster energy and $\sum(p_{\mathrm{T,track}}^{\mathrm{matched}})$ is the sum of the transverse momenta of all tracks matched to the cluster. If $E_{\mathrm{T,cluster}}^{\mathrm{subtracted}} < 0$ the cluster is discarded, otherwise it is assigned energy $E_{\mathrm{T,cluster}}^{\mathrm{subtracted}} > 0$.

To quantify the effect of this correction, one can look at the ratio of the average total energy deposit measured by the EMCal *after* subtraction to the raw energy *before* subtraction, which is shown in fig. 3.13. The effect of using a different fraction, f in the above equation, can be seen by comparing the three curves in fig. 3.13. The fraction of energy subtracted is centrality dependent.

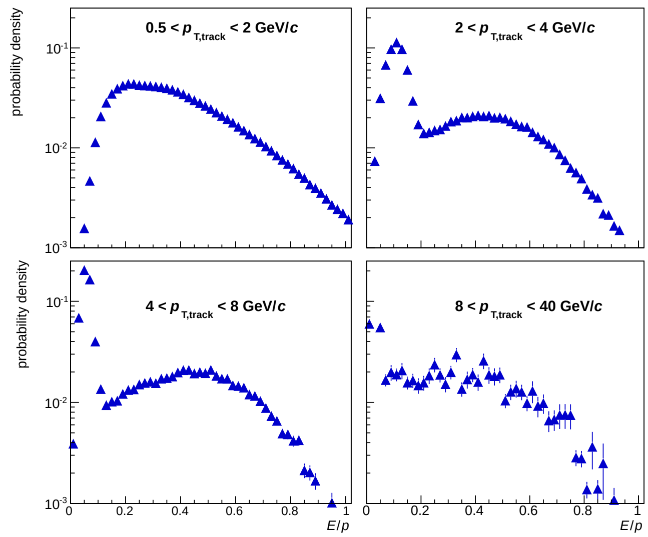

Figure 3.12: EMCal response to charged hadrons (pions). These plots are obtained using a PYTHIA+GEANT3 simulation.

The choice $f = 1.0$ is correct for electrons, but may overestimate the energy deposition due to charged hadrons. If a cluster is generated entirely by charged tracks, the charged track energy is removed accurately from the EMCal without any assumption about the shape of the distribution shown in fig. 3.12. However, if a cluster is generated by both charged tracks and neutral particles, over-subtraction of the charged hadron energy deposition may occur. Nevertheless any choice of $f < 1.0$ may result in a hard-to-determine under-subtraction.

In the final jet spectrum over- and under-subtraction is (partially) corrected on a statistical basis when unfolding detector effects. Indeed the same procedure with the same f parameter is performed in detector-level simulation, so the same "error" is reproduced in the response matrix. This will be discussed more extensively when dealing with systematic uncertainties (see par. 4.5.3).

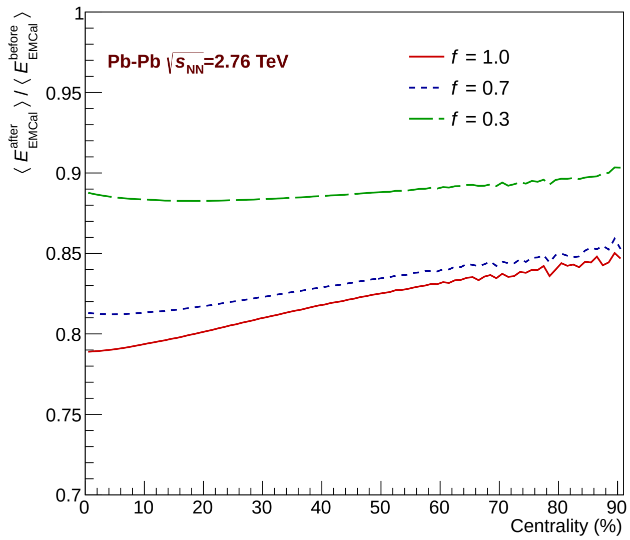

Figure 3.13: This plot shows the ratio between the average total energy deposit measured by the EMCal *after* charged particle correction over the average total energy deposit *before* correction in fine centrality bins. The ratio is shown for three different choices of the fraction f in eq. 3.3.

3.4 Jet finding algorithms and the `FastJet` package

In the very early jet measurements, very simple "jet finding" algorithms were adopted. These algorithms usually looked at some global properties of the event to determine how "jet-like" it appears and compare to jet and non-jet models. For example, Ref. [28] reports one of the first experimental observation of jets in e^+e^- collisions at energies between 3 and 7.4 GeV in the center of mass. In this pioneering measurement the jet finder consisted in the calculation of the eigenvalues of the tensor:

$$T^{\alpha\beta} = \sum_i (\delta^{\alpha\beta}\vec{\mathrm{p}}_i - p_i^\alpha p_i^\beta), \tag{3.4}$$

where $\vec{p}_i$ is the 4-momentum of the i-th particle and α, β are Lorentz indices. It can be proved that the eigenvector of the minimum eigenvalue is the jet axis direction (if there are any in the event), i.e. the direction that minimizes the sum of the square of the transverse momenta of all particles in the given event. To test how "jet-like" the event is, they looked at the variable:

$$S = \frac{3\lambda_3}{\lambda_1 + \lambda_2 + \lambda_3} = \frac{3(\sum_i p_{\perp i}^2)_{\min}}{2\sum_i \vec{p}_i^2}, \tag{3.5}$$

where λ_i are the eigenvalues of the tensor in eq. 3.4. The event distribution of the S variable was compared with the ones obtained from a jet model and from a non-jet model. It turned out that the jet model was able to describe the observed distribution while the non-jet model was not.

As a deeper understanding of the theoretical aspects of hadron production was being accomplished, together with the availability of higher energy collisions and faster computing facilities, more comprehensive jet finding algorithms have been developed, making it possible to actually measure the properties of jets, like their energy and spatial distributions. Insofar as jet-finding is an approximate attempt to invert the quantum mechanical processes of QCD branching and hadronization, it is not a unique procedure.

3.4.1 Jet cone algorithms

The original theoretical definition for jets in e^+e^- collisions was based on grouping particles whose momenta are spatially correlated inside a certain angular cone [29]. Cone jet finders identify energy-flow into cones in pseudorapidity η and azimuth ϕ, together with various steps of iteration, merging and splitting of the cones to obtain the final jets. At first sight they may appear simple, but modern cone jet finders tend to be rather complex.

To find directions of dominant energy flow, cone algorithms usually take some (or all) of the event particles as “seeds”, i.e. trial cone directions. Then for each seed they establish the list of particles in the trial cone, evaluate the sum of their 4-momenta, and use the resulting 4-momentum as a new trial direction for the cone. This procedure is iterated until the cone direction no longer changes, i.e. until one has a “stable cone”. Stable cones have the property that the cone axis a (a 4-vector) coincides with the (4-vector) axis defined by the total momentum of the particles contained in the cone.

Two types of problem arise when using seeds as starting points of an iterative search for stable cones. On one hand, if one only uses particles above some momentum threshold as seeds, then the procedure is collinear unsafe. For example, if a parton undergoes a collinear split, then it may hadronize such that the leading particle is not anymore above threshold, thus changing the seed particle set and the outcome of the jet finding procedure. Alternatively, if any particle can act as a seed then one needs to be sure that the addition of an infinitely soft particle cannot lead to a new (hard) stable cone being found, otherwise the procedure is infrared (IR) unsafe. Infrared safety is a serious issue, not just because it makes it impossible to carry out meaningful (finite) perturbative calculations, but also because it breaks the whole relation between the (Born or low-order) partonic structure of the event and the jets that one observes. It is precisely this relation that a jet algorithm is supposed to codify: it makes no sense for the structure of multi-hundred GeV jets to change radically because hadronization, the underlying event or pileup threw a 1 GeV particle between them. In fact it has been shown that traditional iterative cone algorithms are not IR-safe.

Many workarounds have been proposed in order to avoid that. One consists of adding artificial “midpoint” seeds between pairs or triplets of stable cones. These kinds of algorithms have been frequently used at Tevatron [30, 31].

The midpoint procedure works fine to avoid many of the particle configurations violating infrared safety, but other more complex configurations can still happen. "Seedless" cone jet algorithms, which usually come with a non-iterative approach, have been shown to be Infrared- and Collinear-safe (IRC-safe). The counterpart is that they used to be extremely slow. One of these algorithms, proposed in Ref. [32], takes time $\mathcal{O}(N2^N)$ to find all the stable cones in an event with N particles. This is manageable for a parton-level event with $N \leq 4$, but completely prohibitive at hadron-level with $N \sim 100$: the computational time would be $\sim 10^{17}$ years!

I will focus on two solutions which have been proposed so far in order to ensure IRC-safety and still have reasonable computational time. The first solution is the SISCone algorithm, which is briefly discussed in the next paragraph. The second one consists in using a rather different category of jet finders, which are commonly referred as "successive recombination" algorithms. This is indeed the solution adopted for this analysis.

The SISCone algorithm

A seedless cone algorithm usually starts looking at any subset of particles in the event. The number of all possible subsets for a set of N particles is 2^N. This approach is very inefficient for large N since most of these subsets cannot actually make a trial cone as particles may be too far apart. The basic idea of the SISCone algorithm is to reduce this number by efficiently selecting only those subsets which in principle can form a cone. The way it is done is very simple in the 1-dimensional case and can be easily extended in 2 dimensions. In the 1-dimensional case instead of a circle of radius R in the η, ϕ plane, a line segment of length $2R$ is used. As sketched in fig. 3.14, one first starts putting

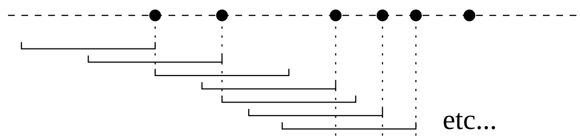

Figure 3.14: Representation of points on a line and the places where a sliding segment has a change in its set of enclosed points.

the segment on the left such that it includes only the leftmost particle. This is indeed the first subset. In the next step the segment is moved to the right an amount which is just sufficient to include the next particle, and so on until the last particle is reached. Then one has to check which of these cones are stable. However the number of cones to check is reduced to N, which is a great improvement compared to 2^N. In the 2-dimensional case it can be proven that one finds all the possible trial cones looking only for circles which have two particles in their boundaries. The maximum number of trial cones is N^2 in this case.

For further details, proofs of IRC-safety and performance comparisons with other algorithms see Ref. [33].

3.4.2 Sequential recombination algorithms

One of the first collaborations which developed and used a successive recombination algorithm to reconstruct jets was the JADE collaboration [34] at DESY. In the following years many variants of the JADE algorithm have been proposed. The Cambridge/Aachen [35], k_{T} [36] and Anti-k_{T} [37] algorithms are amongst the most known ones. To some extent, these definitions are less intuitive, since they do not rely on an immediate "geometric" visualization; nevertheless they are more efficient to overcome the theoretical issues related to the IRC-safety.

To describe how a successive recombination algorithm works we shall start defining a measure:

$$d_{ij} = \min\left(k_{\mathrm{T},i}^{2p}, k_{\mathrm{T},j}^{2p}\right) \frac{\Delta_{ij}^2}{R^2} \tag{3.6a}$$

$$d_{i\mathrm{B}} = k_{\mathrm{T}i}^{2p}, \tag{3.6b}$$

where $\Delta_{ij}^2 = (\eta_i - \eta_j)^2 + (\phi_i - \phi_j)^2$, and $k_{\mathrm{T}i}$, η_i and ϕ_i are respectively the transverse momentum, pseudorapidity and azimuth of particle i. R is a parameter which defines the dimensional scale of the jets that are going to be reconstructed. We shall refer to it as a "radius", though strictly speaking it does not act as a geometrical radius as it does in cone jet finders. The parameter p depends on the particular implementation.

We first calculate all such distances. Then we look for the smallest one. If it is of type d_{ij} then particles i and j are grouped into a "pseudo-jet", i.e. they are removed from the set and a new particle, with a 4-momentum given by the sum of the 4-momenta of the two original ones, is added. Then the distances d_{ij} and $d_{i\mathrm{B}}$ are recomputed and the procedure is iterated. Conversely, if the smallest distance is of type $d_{i\mathrm{B}}$ the i-th particle is removed from the set and declared a jet. Again the procedure is iterated until at least two particles are still in the set.

Different behaviors can be achieved by varying accordingly the p parameter in eqs. 3.6.

The Cambridge/Aachen algorithm

In the Cambridge/Aachen algorithm we set $p = 0$:

$$d_{ij} = \frac{\Delta_{ij}^2}{R^2} \tag{3.7a}$$

$$d_{i\mathrm{B}} = 1. \tag{3.7b}$$

The algorithm becomes purely geometric, as the p_T of the particles does not enter in the measure definition. The clustering starts from the nearest pair and so on until particles which are separated by a distance smaller than the radius R are found. It has to be noted that since the distance is computed between pseudo-jets, and not between particles, jet shapes can be rather irregular, as particles which are farther than $2R$ may be grouped together if there is a continuous "path" of particles between them.

The k_T and Anti-k_T algorithms

In the k_T algorithm we set $p = 1$:

$$d_{ij} = \min\left(k^2_{\mathrm{T},i}, k^2_{\mathrm{T},j}\right) \frac{\Delta^2_{ij}}{R^2} \tag{3.8a}$$

$$d_{i\mathrm{B}} = k^2_{\mathrm{T}i}. \tag{3.8b}$$

As in the Cambridge/Aachen algorithm pairs of particles are grouped when they are found to be near with respect to the radius R. However in this case soft particles are more likely to be grouped first, even if a hard particle is nearer. Further two pseudo-jets i,j may be grouped together even if $\Delta^2_{ij} > R^2$, i.e. the shape of the resulting jets can be even more irregular than in the Cambridge/Aachen algorithm. It has been shown that this algorithm mimics a walk backwards through the QCD branching sequence, which means that reconstructed jets naturally collect most of the particles radiated from an original hard parton. However the adoption of the k_T algorithm in the heavy-ion environment is discouraged because it turns out to be driven by the overwhelming background of soft particles. On the other hand it is exactly this property that makes the heavy-ion k_T "jets" particularly interesting when studying the background itself. Using the k_T algorithm to estimate the background level in heavy-ion jet measurements has been proposed in Ref. [38] and will be discussed more extensively in par. 3.5.

In the Anti-k_T algorithm we set $p = -1$:

$$d_{ij} = \min\left(\frac{1}{k^2_{\mathrm{T},i}}, \frac{1}{k^2_{\mathrm{T},j}}\right)\frac{\Delta^2_{ij}}{R^2} \tag{3.9a}$$

$$d_{i\mathrm{B}} = \frac{1}{k^2_{\mathrm{T}i}}. \tag{3.9b}$$

What is interesting in this algorithm is that it always starts clustering from the highest momentum particles in the event. Then soft particles are "eaten" by high p_T pseudo-jets until they reach a certain size which is determined by the radius R. Jet shapes are much more regular compared to Cambridge/Aachen and k_T algorithms, and are centered around high p_T particles. We may say that this algorithm is "soft-resilient". This property is particularly important in a heavy-ion environment, where the soft particle component coming from the underlying event is dominant. Indeed we want to reduce the influence of the underlying event in the jet finding procedure. For this reason the Anti-k_T algorithm has been chosen as the standard by many high-energy heavy-ion experiments [24].

Fig. 3.15 shows four event displays of the same parton-level simulated event, clustered with different jet finder algorithms. The active area is determined through the "ghost" particle method which is explained below. Note the very irregular shapes of the Cambridge/Aachen and k_T jets. Though the algorithms are very different, SISCone and Anti-k_T jet collections are rather similar. The main difference is in the way they deal with overlapping jets, which can be appreciated looking at the purple and green jets: SISCone divides the jet geometrically in two halves, while Anti-k_T makes a roundish jet around the highest particle and the rest goes into an irregular jet.

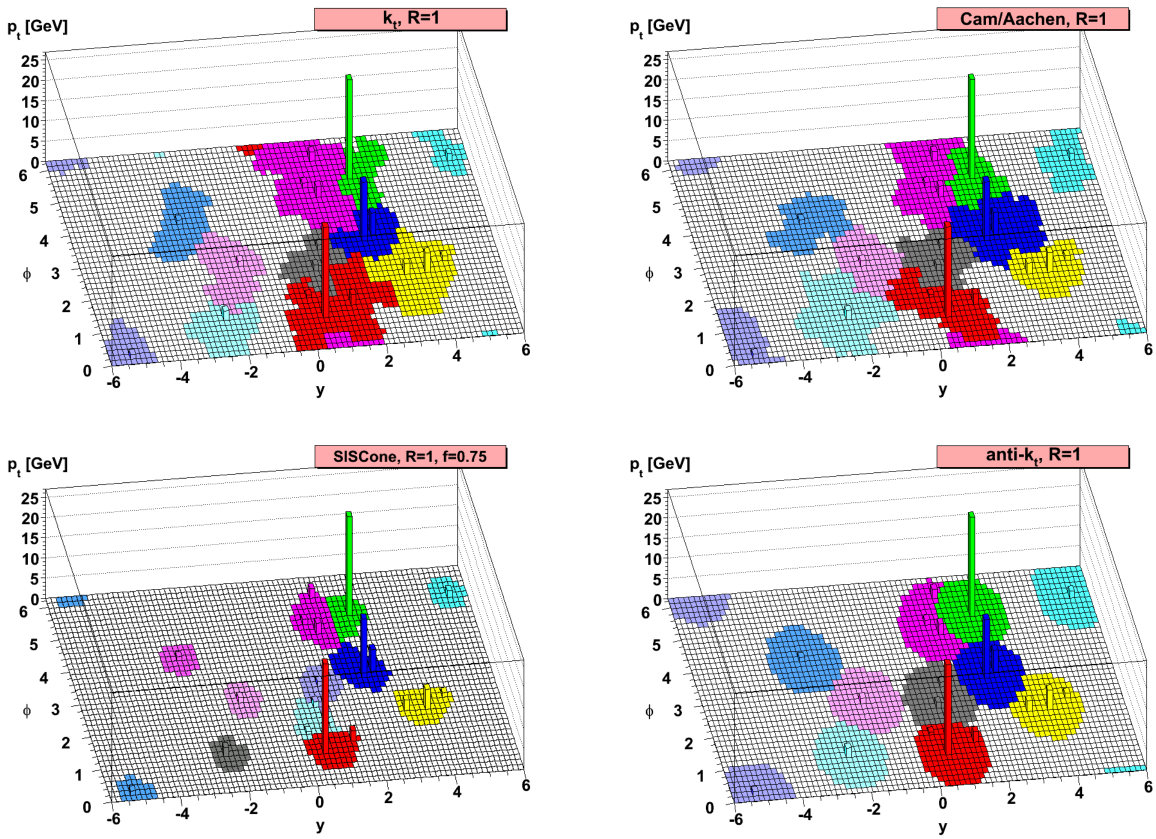

Figure 3.15: A sample parton-level event (generated with Herwig [39]), together with many random soft "ghosts", clustered with four different jets algorithms, illustrating the "active" catchment areas of the resulting hard jets.

The FastJet package

Previously, successive recombination algorithms were not commonly used at hadron colliders, due to their slowness. In fact in the first implementations the execution time grew as $\mathcal{O}(N^3)$, where N is the number of particles. The computational time per event (pp or $p\bar{p}$)

for a modern CPU (3 GHz) would be $\sim$ 10 s at the Tevatron and $\sim 10^5$ s at the LHC. More recently [40], faster implementations have been developed with a considerably decreased execution time.

In this analysis the `FastJet` [41] package has been employed. It contains a fast `C++` implementation of many of the most common jet algorithms, including the Cambridge/Aachen, the k_{T} and the Anti-k_{T} algorithms and, through an external plugin, the SISCone algorithm. It also provides a powerful definition of the jet area, which is very useful to compute and subtract the background (the background subtraction procedure is explained in par. 3.5).

Jet area definition

The jet area is not a trivially defined concept, especially when dealing with successive recombination algorithms. In Ref. [42] the following two different definitions of area have been proposed:

Active area A uniform background of extremely soft massless "ghost" particles is added to the event. Ghost particles participate in the clustering together with the reconstructed particles. The area of a given jet is proportional to the number of ghosts it contains. Because the ghosts are extremely soft, the presence of the ghosts does not affect the clustering itself, provided that the algorithm is IR-safe.

Passive area A single randomly placed ghost at a time is included to the event. One examines which jet (if any) the ghost ends up in. One repeats the procedure many times and the passive area of a jet is then proportional to the probability of the jet containing the ghost.

The area can be calculated either as a scalar, or as a 4-vector. Essentially the scalar case corresponds to counting the number of ghosts in the jet, while the 4-vector case corresponds to summing their 4-vectors (normalized such that for a narrow jet, the transverse component of the 4-vector is equal to the scalar area).

These area definitions are implemented in `FastJet`. In this analysis the "active area" definition has been employed.

3.5 Underlying event subtraction

Jet measurements in heavy-ion collision are particularly challenging because of the large amount of background given by the underlying event (UE), produced simultaneously with the hard nucleon-nucleon collision that creates the high-transverse momentum jet. There exists no unambiguous conceptual definition of the UE. However we can define it as the low transverse momentum part of the event that is not naturally associated with the partonic hard scattering.

UE is also present in pp collisions, though it is not precisely due to the same mechanisms as in heavy-ion collisions. Many studies have been devoted to its characterization [43, 44]. Different phenomenological models have been proposed to account for it, the most successful ones involving multiple $2 \to 2$ scattering ("multiple parton interactions", MPI), as sketched in fig. 3.16a. Other physics processes that may contribute to the UE are represented in figs. 3.16b-d.

While in pp collision the contribution of the UE to the reconstructed jet p_{T} can be considered negligible[1] in the first order – the background density ρ being a few GeV/c per unit area [44] – in Pb–Pb collision it can account for a large fraction (up to 50% for $R = 0.4$) of the reconstructed jet p_{T}.

The UE contribution to the jet reconstructed p_{T} needs to be prop-

[1]In case of very high luminosity, like for CMS and ATLAS, up to about 20 pp interactions happen within a bunch crossing; this translates in a higher background level that can reach densities $\rho_{\mathrm{pp}} \sim 10 - 20$ GeV/c per unit area [38].

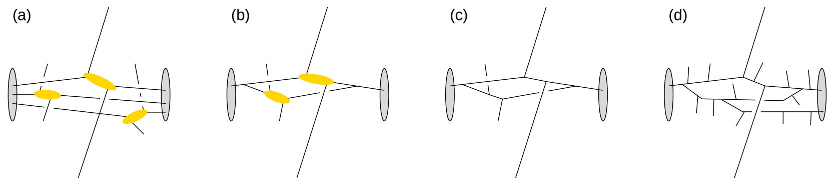

Figure 3.16: Views of a hard scattering plus UE; (a) multiple $2 \to 2$ interactions, as incorporated in the most successful models; (b) collinear splitting in the initial-state in a double $2 \to 2$ scattering; (c) perturbative 1-loop $2 \to 4$ diagram; (d) example of multiple chains with low-$p_{\rm T}$emissions spread in rapidity.

erly estimated and subtracted in order to have a clean measurement of its "true" momentum, i.e. the one it would have in the absence of the UE contribution. The method used for this analysis, which I shall describe in what follows, consists of two separate steps: an average background subtraction, which is done jet-by-jet; and a background fluctuation correction which is applied to the reconstructed spectrum on a statistical basis through unfolding (see par. 3.7).

I shall first focus on the charged-only case; then the more specific aspects related to the inclusion of the electromagnetic calorimeter in the analysis will be addressed.

3.5.1 Average background subtraction

The main problem in the estimation of the average background deals with the separation of the UE from the hard scattering. There is no obvious way to accomplish this task, and any background estimation will always be influenced to some extent by the hard scattering part of the event.

The simplest method to estimate the background is to use all the reconstructed particles to compute the average $p_{\rm T}$ density per unit area in the (η, ϕ) plane for a given event. This method can be refined to reduce the contribution from the hard scattering, removing one or two of the particles with the highest p_{T} (which most likely are associated to a hard scattering process).

Other, more sophisticated methods have been proposed in the last years to reduce further the contribution from the hard scattering.

Cacciari et al. have recently proposed [38] a method that makes use of some particular jet finding algorithms to estimate the background. In that paper they claim that the k_{T} and the Cambridge/Aachen algorithms are particularly suitable for this purpose because they show the tendency to naturally organize a uniform background of soft particles into structures ("jets") each of area $\sim \pi R^2$. The proposed method consists of taking the median value of the distribution of $p_{\mathrm{T}j}/A_j$ to estimate ρ event-by-event:

$$\rho = \mathrm{median}\left[\left\{\frac{p_{\mathrm{T}j}}{A_j}\right\}\right] \tag{3.10}$$

where $p_{\mathrm{T}j}$ and A_j are respectively the transverse momentum and the area of the jet j. Three conditions should hold for this procedure to be valid:

1. The background noise should be independent of rapidity and azimuth.

2. The radius R of the jet finding algorithm should be no smaller than the typical distance between particles, otherwise the extraction of ρ will be biased by the large amount of empty space not associated with jets.

3. The number of jets made of background particles should be much larger than the number of jets from the hard interaction that are above scale $A\rho$,

$$N_{\mathrm{jet_{UE}}} \gg N_{\mathrm{jet_H}}^{p_{\mathrm{T}}>A\rho}. \tag{3.11}$$

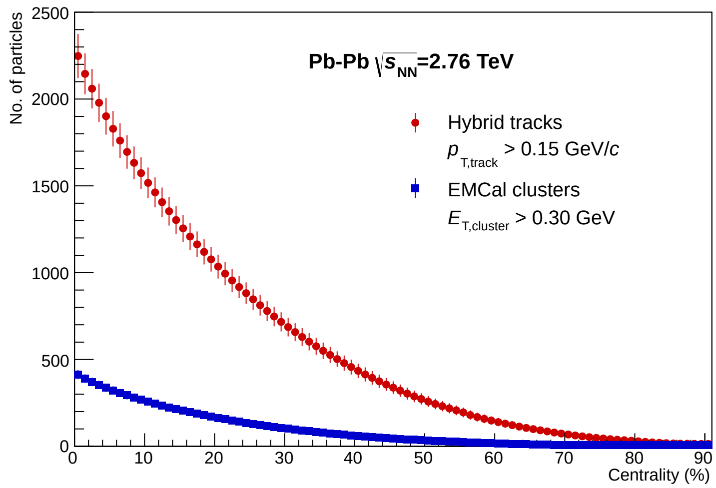

Figure 3.17: Number of hybrid tracks (red) and number of EMCal clusters (blue) as a function of centrality.

It is well known that particles coming from heavy-ion collisions are not evenly distributed in (pseudo)rapidity. However this effect becomes important only at forward rapidity. In the mid-rapidity range, in which this analysis is focused, the particle distribution is roughly flat (see fig. 3.4) and non-uniformities are to be considered as a second or higher order effect. Non-uniformities in the azimuthal distribution are due to flow [45]. Again this can be considered a higher order effect, especially in the most central collisions where flow plays a smaller role. Non-uniformities in the background density throw in additional fluctuations, which are corrected afterwards. A bias towards flow-dominated background might appear when a minimum leading hadron p_{T} requirement is included in the jet definition. This will be discussed below.

The number N_{ch} of reconstructed charged tracks in central (0-10%) Pb-Pb collisions ranges from 1400 to 2600 (see fig. 3.17). The area of the TPC is $A_{\mathrm{TPC}} = \Delta\eta \times \Delta\phi = 1.8 \times 2\pi \approx 11.3$, which gives a particle

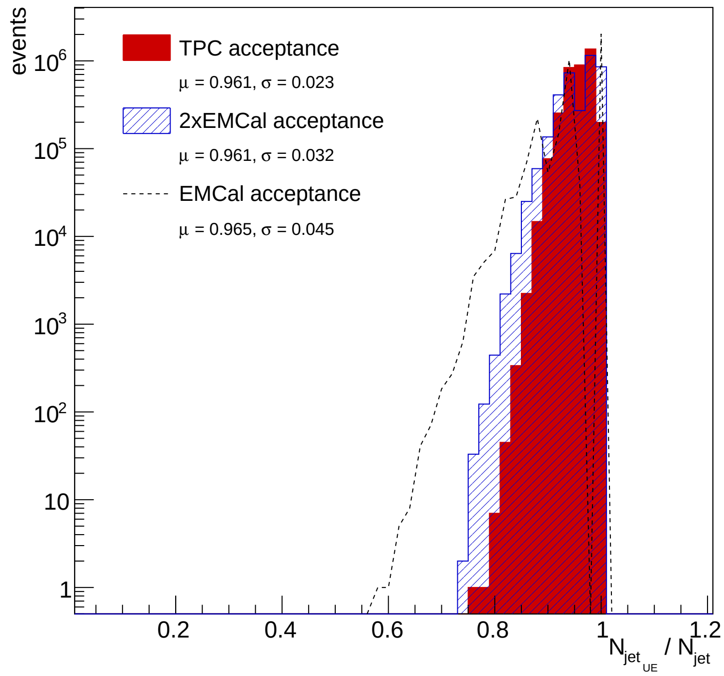

Figure 3.18: Event distribution of the ratio $N_{\text{jet}_{\text{UE}}}/N_{\text{jet}}$ for charged jets in TPC acceptance (red filled area), 2 × EMCal acceptance (blue shadowed area) and EMCal acceptance (black dotted line). The average background ρ_{charged} is calculated as in eq. 3.10 using the k_{T} algorithm with R=0.2. See text for details about the definition of $N_{\text{jet}_{\text{UE}}}$ and N_{jet}.

density

$$n_{\text{ch}} = \frac{N_{\text{ch}}}{A_{\text{TPC}}} \approx 124 \div 230. \tag{3.12}$$

Assuming that the particles are uniformly distributed in the (η, ϕ) plane (which is not exactly true for flow particles and, of course, for jets) the typical distance between particles can be estimated as:

$$d_{\text{ch}} = \sqrt{\frac{1}{n_{\text{ch}}}} \approx 0.09 \div 0.07 \tag{3.13}$$

which means $R > 0.1$.

We now move to condition 3. The red filled area in fig. 3.18 shows the event distribution of the ratio $N_{\mathrm{jet_{UE,ch}}}/N_{\mathrm{jet_{ch}}}$, where $N_{\mathrm{jet_{H,ch}}}$ is the number of jets above the event background scale, $p^{ch}_{\mathrm{T,jet_H}} > p^{\mathrm{ch}}_{\mathrm{T,bkg}}$; $N_{\mathrm{jet_{ch}}}$ is the total number of reconstructed jets and $N_{\mathrm{jet_{UE,ch}}} = N_{\mathrm{jet_{ch}}} - N_{\mathrm{jet_{H,ch}}}$. To define properly a background scale one cannot just set $p^{\mathrm{ch}}_{\mathrm{T,bkg}} = A\rho_{\mathrm{ch}}$, because the background is described by a distribution, of which $A\rho_{\mathrm{ch}}$ is the mean value. As it will be discussed in par. 3.5.2 there exist different methods to probe the width of this distribution[2]. For $R = 0.2$, $\sigma_{\rho_{\mathrm{ch}}} \approx 35.83$ GeV/c. We can then define a background p_{T} scale as:

$$p^{\mathrm{ch}}_{\mathrm{T,bkg}} = A \times (\rho_{\mathrm{ch}} + 3\sigma_{\rho_{\mathrm{ch}}}) \tag{3.14}$$

which has the meaning that 99% of the k_{T} jets should be below that scale, if the contamination from the hard scattering is negligible. The distribution of the variable $N_{\mathrm{jet_{UE,ch}}}/N_{\mathrm{jet_{ch}}}$ from fig. 3.18 is quite broad but it never goes below 0.8.

Background subtraction for full jet reconstruction

Full jet reconstruction with the EMCal needs some particular attention. In principle the problem of the estimation of the UE should be completely equivalent. However due to the limited acceptance of the calorimeter in ALICE the same procedure cannot be followed as it is. In fact, even for $R = 0.2$ the average number of jets per event within EMCal acceptance is $N^{\mathrm{EMCal}}_{\mathrm{jet}} \approx 18$ which is considerably lower compared to the number of charged jets in the TPC acceptance, $N^{\mathrm{TPC}}_{\mathrm{jet}} \approx 77$ (see fig. 3.19). The distribution of the variable $N_{\mathrm{jet_{UE}}}/N_{\mathrm{jet}}$ for EMCal full jets (dotted line in fig. 3.18) is broader and can go as low as $0.6 \div 0.7$. So we expect a stronger bias from jet fragments. To avoid this bias one can instead use ρ_{charged} multiplied by a scaling factor to account for the

[2]We cannot just use the width from fig. 3.21 because that is an "event-by-event" distribution, while what we need for this calculation is a "within-event" $\sigma_{\rho_{\mathrm{ch}}}$.

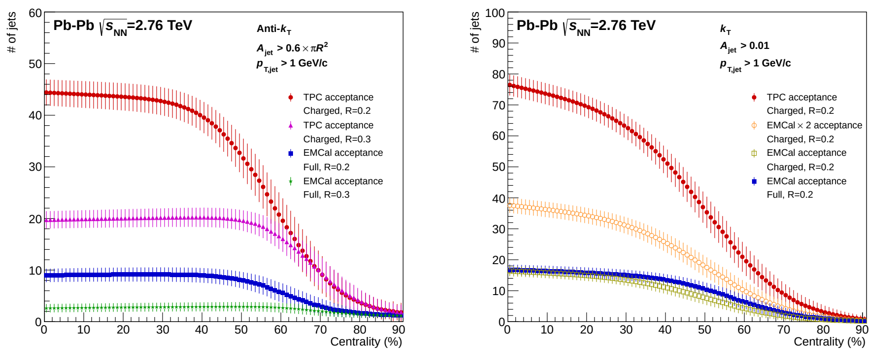

(a) *Anti-*k_T *with* $R = 0.2, 0.3$.

(b) k_T *with* $R = 0.2$.

Figure 3.19: Average number of reconstructed jets per event as a function of centrality for different algorithms, radii and acceptances.

neutral energy contribution. About 1/3 of the total energy released in a binary high energy collision is carried by neutral particles. However due to the reconstruction efficiency, which is not the same for charged and neutral particles, this scale factor is detector-specific and needs to be determined experimentally.

In practice due to the "hole" in the TPC only a reduced acceptance has been used to calculate both ρ_charged and the scale factor. This region corresponds roughly to twice the EMCal acceptance (see fig. 3.5). The scale factor s_EMC is calculated as the sum of the p_T of all reconstructed clusters and charged tracks, corrected for their respective acceptances, over the sum of the p_T of all reconstructed charged tracks, times the acceptance of the reduced TPC:

$$s_\mathrm{EMC} = \frac{\sum_i E^i_\mathrm{T,clusters}/A_\mathrm{EMC} + \sum_j p^j_\mathrm{T,tracks}/A_{\mathrm{TPC}_\mathrm{red}}}{\sum_j p^j_\mathrm{T,tracks}} \times A_{\mathrm{TPC}_\mathrm{red}} \quad (3.15)$$

The scale factor s_EMC depends slightly on the centrality (see fig. 3.20).

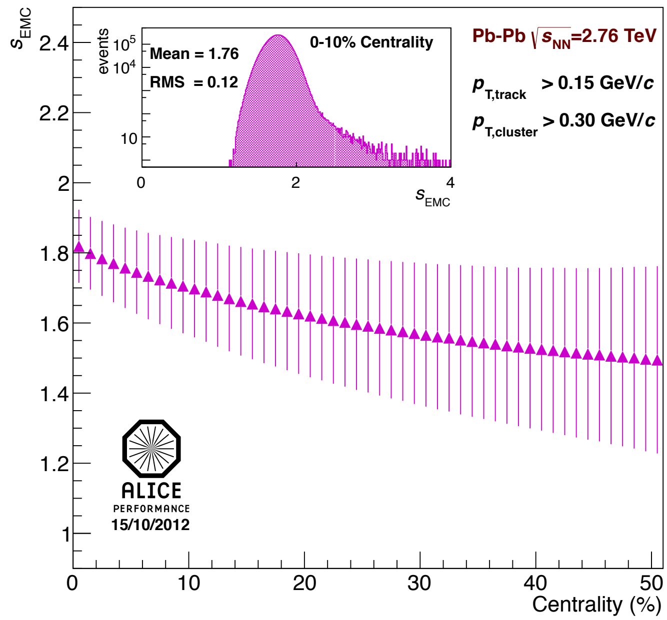

Figure 3.20: Scale factor s_{EMC} as a function of centrality.

Fig. 3.21 shows the ρ distribution. The k_{T} algorithm with $R = 0.2$ is run over all reconstructed tracks with $|\eta| < 0.9$, while only jets within a fiducial acceptance ($|\eta| < 0.5$) are selected. The average background ρ_{charged} is calculated as in eq. 3.10; ρ_{scaled} is obtained from ρ_{charged} event-by-event:

$$\rho_{\mathrm{scaled}} = \rho_{\mathrm{charged}} \times s_{\mathrm{EMC}} \tag{3.16}$$

Fig. 3.21b also shows $\rho_{\mathrm{ch+ne}}$, i.e. the average background calculated using tracks and clusters in the EMCal acceptance: the longer tail in the right-hand-side is an indication of a stronger bias from jet fragments.

3.5.2 Background fluctuations estimation

Background fluctuations are the largest source of uncertainty in the measurement. This is because the jet spectrum is a steeply falling

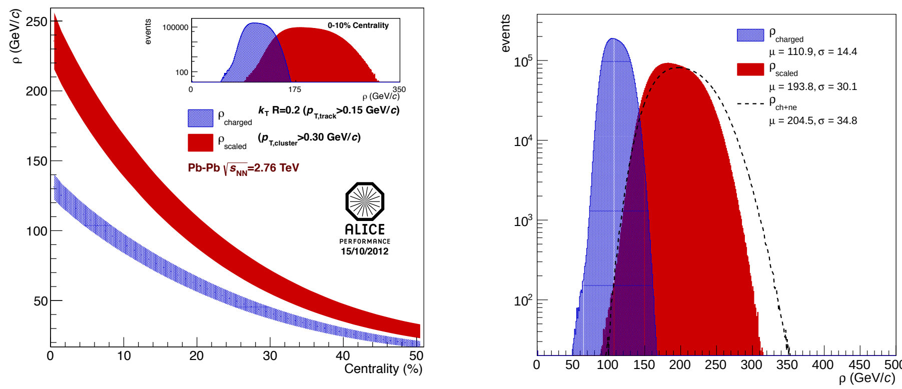

(a) ρ *vs. centrality.* (b) *0-10% centrality class.*

Figure 3.21: Average background ρ distribution: ρ_{charged} (blue), ρ_{scaled} (red) and $\rho_{\text{ch+ne}}$ (dotted black line), only shown in the 0-10% centrality class.

function of the p_{T} and fluctuations in the background density may have a big effect in its shape, especially for larger jet cone radii.

Background fluctuations have been estimated in two different ways, one of which is independent of the particular jet finder choice (apart from the jet area scale), while the other makes use of the same algorithm employed to reconstruct signal jets.

The first method, which is often referred as "unbiased" method, throws a random η, ϕ direction in the fiducial acceptance (the same used for signal jets) and sum up the p_{T} of all reconstructed particles in a cone of radius R ("random cones", RC). A δp_{T} distribution is built according to the following formula:

$$\delta p_{\text{T}}^{\text{RC}} = p_{\text{T}}^{\text{RC}} - \rho \times \pi R^2. \tag{3.17}$$

The second method consists in running the same jet finder algorithm as for signal jets after embedding in every event a high p_{T} particle or even a jet. In this case the δp_{T} distribution is built according to the

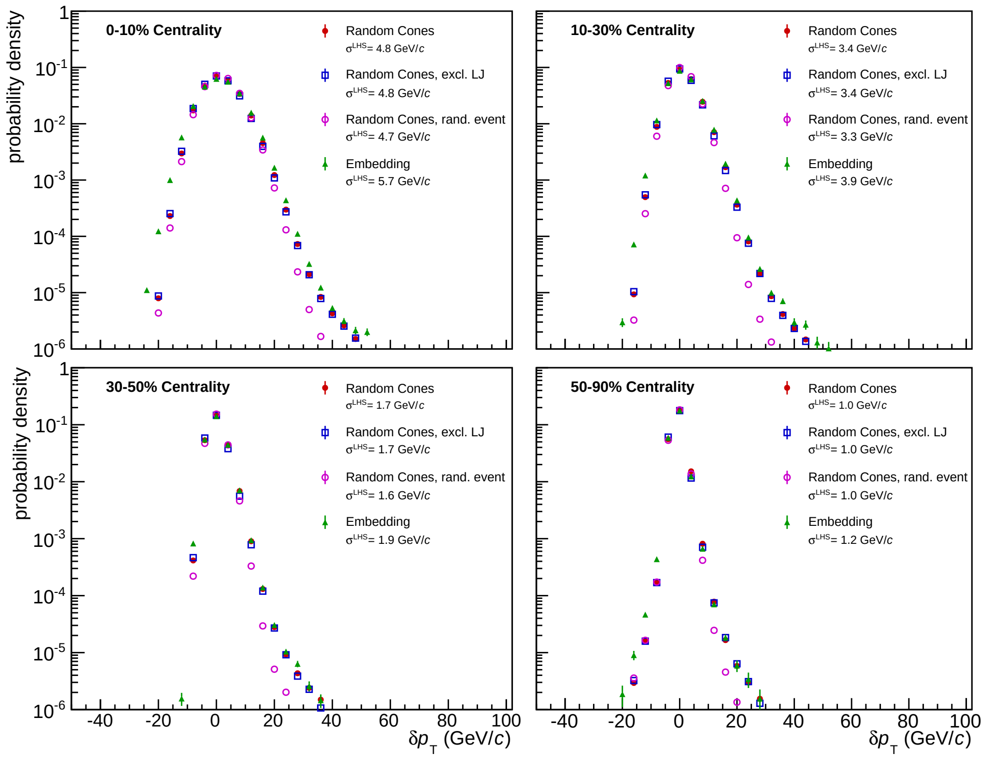

Figure 3.22: δp_{T} distributions with $R = 0.2$ obtained with different methods and for different centrality classes.

formula:

$$\delta p_{\mathrm{T}}^{\mathrm{emb}} = p_{\mathrm{T,jet}} - p_{\mathrm{T,probe}} - \rho \times A_{\mathrm{jet}}, \tag{3.18}$$

where $p_{\mathrm{T,probe}}$ is the p_{T} of the embedded particle or jet.

Azimuth (and rapidity) randomized events can be used to estimate the contributions to fluctuations arising from uncorrelated sources with respect to the correlated sources (flow, jets,...). One can also impose a minimum distance from the higher-p_{T} jet in the event to probe the fluctuations in a region which is far from where the hard collision released most of the energy. Fig. 3.22 and 3.23 show δp_{T} distributions for full jets in the EMCal fiducial acceptance with two different jet cone

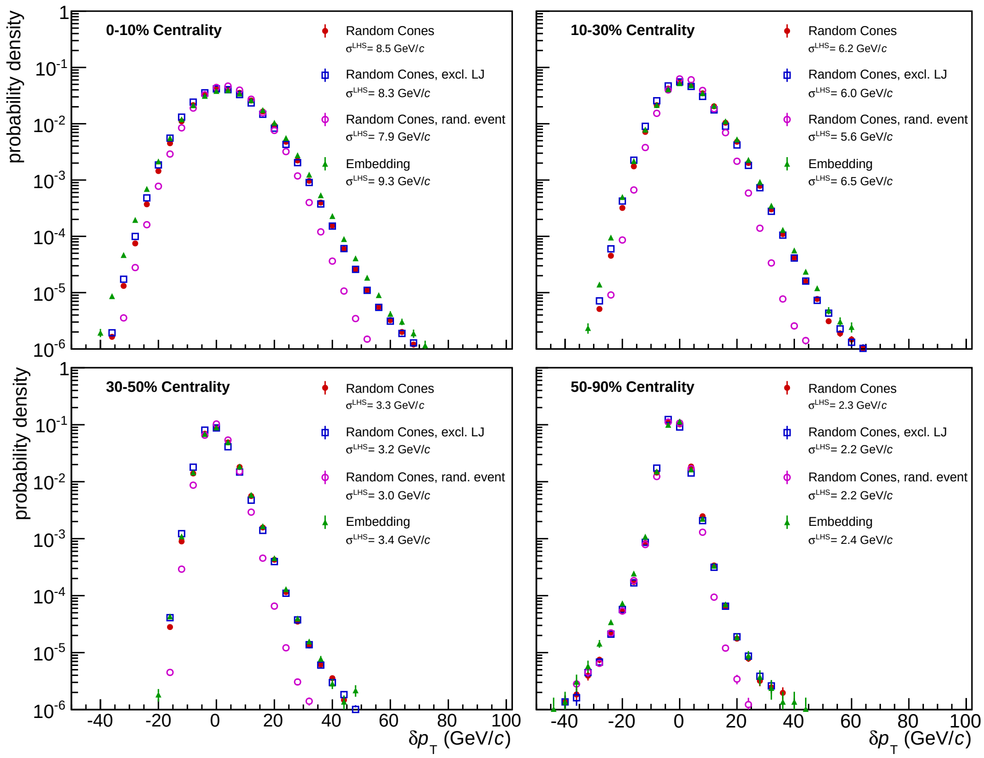

Figure 3.23: δp_{T} distributions with $R = 0.3$ obtained with different methods and for different centrality classes.

radii (R=0.2, 0.3).

Flow bias

The effect of flow is not taken into account in the average background estimation. In the inclusive jet spectrum it is expected to simply act an additional source of region-by-region fluctuations. On the other hand, in biased spectra, where a minimum leading hadron p_{T} is required, there might be a bias towards flow-dominated background. This effect has been studied using δp_{T} distributions where a track with a minimum p_{T} was required to be contained within the EMCal accep-

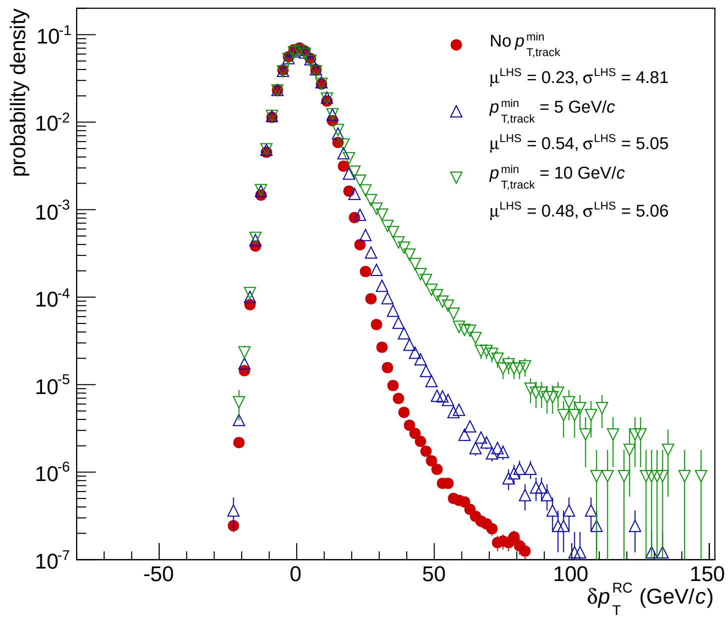

Figure 3.24: $\delta p_{\rm T}$ distributions obtained with the "random cones" method: no additional requirement (red), $p_{\rm T,track}^{\rm min} = 5$ GeV/c (blue), $p_{\rm T,track}^{\rm min} = 10$ GeV/c (green).

tance. This is shown in fig. 3.24. The right hand side (RHS) is dominated by signal jet fragments, and, as expected, is much more enhanced when a high-momentum track was required to be contained within the EMCal acceptance. Interestingly enough, the left hand side (LHS) is only slightly affected by this requirement, which is indeed consistent with the assumption that the LHS is dominated by the UE, with very small or null contribution from hard scattering. In fact regions with dense transverse momentum ("jets") are expected to stick out from the average background, thus appearing only in the RHS of the $\delta p_{\rm T}$ distribution. So the shift of the mean of LHS of this distribution, due to the requirement of a high-$p_{\rm T}$ track, gives an estimate of the background flow bias. The mean of the LHS is calculated by iteratively fitting the distribution in the range $(\mu^{\mathrm{LHS}} - 3\sigma^{\mathrm{LHS}}, \mu^{\mathrm{LHS}} + 0.5\sigma^{\mathrm{LHS}})$ with a Gaussian function, until the parameters of the fit become stable. The observed shift is 310 MeV/c for $p_{\mathrm{T,track}}^{\mathrm{min}} = 5$ GeV/c and 250 MeV/c for $p_{\mathrm{T,track}}^{\mathrm{min}} = 10$ GeV/c which are very small compared to the widths of the distributions (~ 5 GeV/c).

3.6 Detector response

The detector response to jet reconstruction has been studied with *Monte Carlo* simulated events. About 12 millions proton-proton events at $\sqrt{s} = 2.76$ GeV/c have been simulated using the PYTHIA6 [46] Jet-Jet event generator. Each simulated p_{T} hard bin (ranging from 5 GeV/c to infinity) has been weighted by the cross section in minimum bias. The detector response has been simulated using the GEANT3 [47] transport code. An accurate description of the detector, including the specific detector configuration (voltages, magnets, etc.) used at the time of data taking, is employed. Simulated events are reconstructed using the same framework and parameters as it is done for real events.

In addition, to account for the reduced tracking efficiency due to the higher multiplicity in Pb–Pb collisions, 5% of the tracks have been removed at detector level. Apart from this correction for the tracking efficiency, the detector response to jet reconstruction is assumed to be the same as in proton-proton collisions.

In order to apply a meaningful correction to the final spectra, a jet reconstruction with the same parameters (except the background subtraction, which is assumed to be negligible in pp collisions) is performed both at particle and detector level simulation. Jets belonging to the two levels of the same event are matched following a geometrical criterion. Particle-level jet A is matched with detector-level jet B if:

– $d(\mathrm{A},\mathrm{B}) = \sqrt{(\eta_{\mathrm{A}} - \eta_{\mathrm{B}})^2 + (\phi_{\mathrm{A}} - \phi_{\mathrm{B}})^2} < 0.25$;

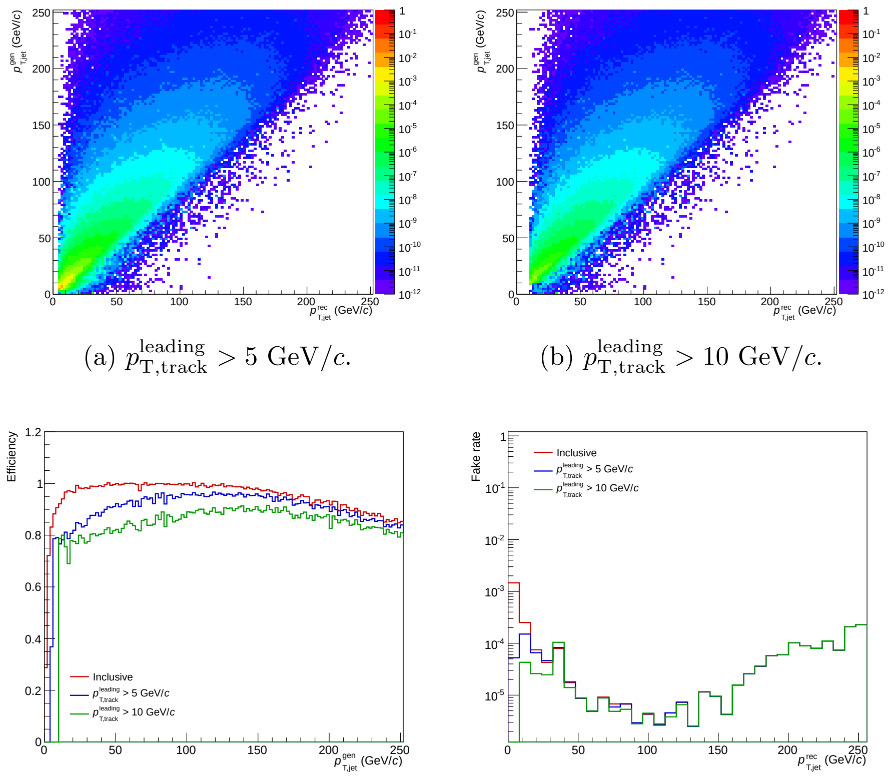

(a) $p_{\mathrm{T,track}}^{\mathrm{leading}} > 5$ GeV/c.

(b) $p_{\mathrm{T,track}}^{\mathrm{leading}} > 10$ GeV/c.

(c) *Jet detector efficiency.*

(d) *Fake rate.*

Figure 3.25: Detector jet response simulation (PYTHIA+GEANT3) for $R = 0.2$.

– A is the nearest particle-level jet to B and B is the nearest detector-level jet to A (in the sense of the distance defined above).

It has to be noted that fiducial acceptance cuts, track quality cuts (e.g. maximum track p_{T} accepted) and any minimum leading hadron p_{T} requirement are *not* applied at particle level, although they are at detector level.

When a valid matching is found, an entry is added to a fine-binned 2-dimensional histogram, having $p_{\mathrm{T,jet}}^{\mathrm{rec}}$ (reconstructed jet p_{T}) in the x axis and $p_{\mathrm{T,jet}}^{\mathrm{gen}}$ (generated jet p_{T}) in the y axis. The resulting histograms

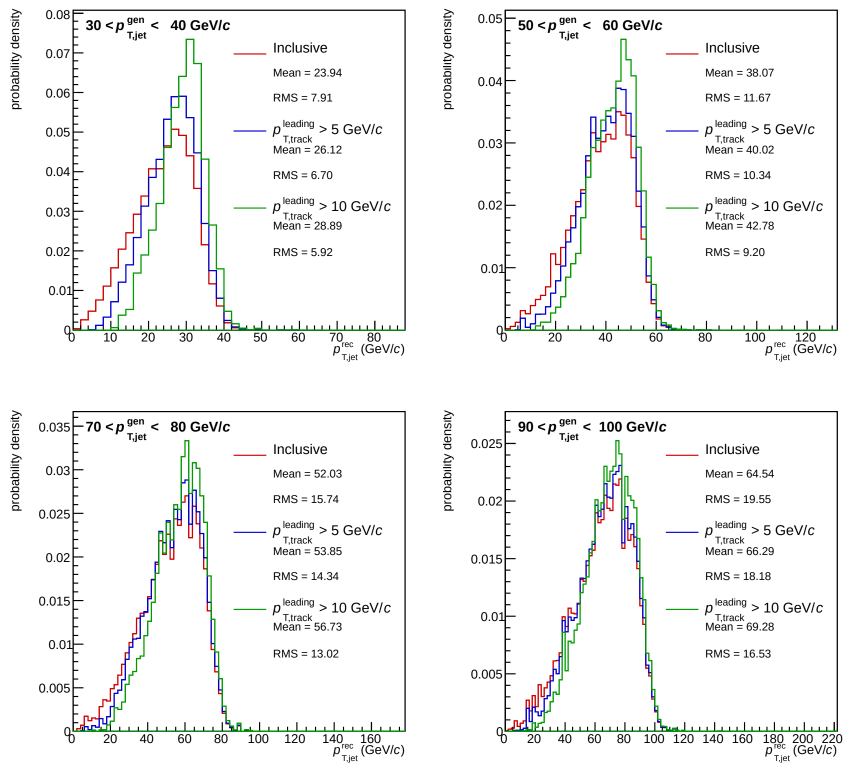

Figure 3.26: Jet p_{T} resolution for different slice of the generated jet p_{T}: inclusive (red); $p_{\mathrm{T,track}}^{\mathrm{leading}} > 5$ GeV/c (blue); $p_{\mathrm{T,track}}^{\mathrm{leading}} > 10$ GeV/c (green).

are shown in fig. 3.25 for $R = 0.2$ and for different leading hadron p_{T} requirements. Projecting a narrow slice of the generated p_{T} axis onto the reconstructed p_{T} axis one can extract the jet momentum resolution and the jet energy scale shift. Such projections are shown in figs. 3.26. The shift of the jet energy scale is mainly due to tracking inefficiency and to unreconstructed neutral particles which flow out of the detector (neutrons, K_L^0, neutrinos,...).

The jet reconstruction efficiency (fig. 3.25c) is defined as follows:

$$\epsilon(p_{\mathrm{T,jet}}^{\mathrm{gen}}) = \frac{N_{\mathrm{jets}}^{\mathrm{matched}}}{N_{\mathrm{jets}}^{\mathrm{all}}}, \tag{3.19}$$

where $N_{\text{jets}}^{\text{matched}}$ are the matched particle-level jets (projection of the matrix in fig. 3.25 onto the y axis) and $N_{\text{jets}}^{\text{all}}$ are all particle-level jets which pass the selection criteria (fiducial acceptance cuts and minimum leading hadron requirement). As the numerator is not an exact subset of the denominator, strictly speaking this is not an efficiency in the traditional definition, so we should rather call it a "generalized" efficiency.

The matrix in fig. 3.25, after proper rebinning, is used in the unfolding procedure (described in the next paragraph) to correct the raw p_{T} jet spectra.

3.7 Unfolding

3.7.1 Definition of the problem

A jet p_{T} spectrum is basically a measurement of a probability density function (pdf). The observable is the transverse momentum of the jets produced in the heavy-ion (pp) collisions of interest. We want to know what is the expectation value μ_j of the number of entries which should go in every bin of a certain p_{T} range. This is often referred to simply as the "true histogram". The sum is denoted by $\mu_{tot} = \sum_i \mu_i$, and the probability for $p_{\text{T,jet}}$ to be found in i is thus $p_i = \mu_i/\mu_{tot}$.

The goal of unfolding is to construct estimators for the M parameters $\boldsymbol{\mu} = (\mu_1, \ldots, \mu_M)$, or alternatively for the probabilities $\boldsymbol{p}$. The non-trivial aspect of this problem[3] arises when the measured values of the observable, the jet p_{T}, are subject to further random fluctuations because of measurement errors. That is, each observation is characterized by a true (and unknown) value, $p_{\text{T,jet}}^{\text{true}}$, and by a measured value,

[3]The trivial part being related to the gaussian fluctuations in each bin which are also present in a simple counting experiment.

$p_{\mathrm{T,jet}}^{\mathrm{meas}}$. The pdfs for $p_{\mathrm{T,jet}}^{\mathrm{true}}$ and $p_{\mathrm{T,jet}}^{\mathrm{meas}}$ are related by a convolution

$$f^{\mathrm{meas}}(p_{\mathrm{T}}^{\mathrm{meas}}) = \int R(p_{\mathrm{T}}^{\mathrm{meas}}|p_{\mathrm{T}}^{\mathrm{true}}) f^{\mathrm{true}}(p_{\mathrm{T}}^{\mathrm{true}}) dp_{\mathrm{T}}^{\mathrm{true}} \tag{3.20}$$

where $R(p_{\mathrm{T}}^{\mathrm{meas}}|p_{\mathrm{T}}^{\mathrm{true}})$ is the response function. This depends on the measuring apparatus and possibly also on some secondary physics processes which may interfere with the measurement (e.g. smearing due to UE). When we consider the usual case where the pdfs of $p_{\mathrm{T,jet}}^{\mathrm{meas}}$ and $p_{\mathrm{T,jet}}^{\mathrm{true}}$ are both represented as histograms, eq. 3.20 becomes:

$$\nu_i = \textstyle\sum_{j=1}^{M} R_{ij}\mu_j, \quad i = 1, \ldots, N, \tag{3.21}$$

where $\boldsymbol{\mu} = (\mu_1, \ldots, \mu_M)$ gives the expectation values for the histogram of $p_{\mathrm{T}}^{\mathrm{true}}$ and $\boldsymbol{\nu} = (\nu_1, \ldots, \nu_M)$ gives the expected number of events in bins of the observed variable $p_{\mathrm{T,jet}}^{\mathrm{meas}}$. The actual data are given as a vector of numbers $\boldsymbol{n} = (n_1, \ldots, n_N)$. These represent the actual (integer) number of entries observed in the histogram, which of course differ in general from the (non-integer) expectation values $\boldsymbol{\nu}$. The *response matrix* R has the simple interpretation as a conditional probability:

$$R_{ij} = P(\text{observed in bin } i \mid \text{true value in bin } j). \tag{3.22}$$

By summing R_{ij} over all possible bins of the observed value i, one obtains the efficiency

$$\epsilon_j = \sum_{i=1}^{N} R_{ij} = P(\text{observed anywhere} \mid \text{true value in bin } j). \tag{3.23}$$

3.7.2 Why unfolding

One often needs to compare measurements, which are given in terms of the observed $\boldsymbol{n}$, with models, which provide the expectation values $\boldsymbol{\mu}^{\mathrm{model}}$. Apparently a direct comparison is not possible. Unfolding is the attempt to extract the expectation values $\boldsymbol{\mu}$ from the measured data.

It is probably worth to note that unfolding is not the only way to compare measurements with models. One could also use the response matrix to include detector effects in the model predictions, computing:

$$\nu_i^{\text{model}} = \sum_{j=1}^{M} R_{ij} \mu_j^{\text{model}}, \tag{3.24}$$

for which a direct comparison with measured data is possible. This procedure is considerably simpler than unfolding the measurement and comparing it with the original (unmodified) theory.

Nevertheless the advantages of unfolding are obvious when one wants to compare results from different experiments, for which the response matrices will be different. In this case unfolding is necessary for the comparison to be meaningful. Further, after unfolding, the result has a more "fundamental" character and can be compared to models which are developed afterwards. Finally in heavy-ion experiments one usually wants to compare with pp or pA results. It may happen that the detector is operated in a slightly different way, which makes unfolding unavoidable.

3.7.3 Regularized unfolding

Suppose the response matrix can be inverted (generally possible in practice) so we can write

$$\boldsymbol{\mu} = R^{-1} \boldsymbol{\nu}. \tag{3.25}$$

In the limit that the components of the data vector $\boldsymbol{n}$ are independent and Poisson distributed it can be shown that the maximum likelihood estimators for $\boldsymbol{\nu}$ are $\boldsymbol{n}$, and thus we can take for estimators of $\boldsymbol{\mu}$,

$$\hat{\boldsymbol{\mu}} = R^{-1} \boldsymbol{n}. \tag{3.26}$$

If the off-diagonal elements of the response matrix are too large, i.e., if the bin size is too small compared to the measurement resolution, then the ML estimators from eq. 3.26 have catastrophically large variances (statistical uncertainty) and strong negative correlations between neighboring bins. One can naively understand the reason of this strange behavior by considering a case in which the true histogram has a very fine structure: after “folding” this histogram with the response matrix, the fine structure will be mostly washed out. So it is clear that, from a mathematical point of view, wild bin-by-bin fluctuations in the unfolded spectrum make perfect sense, even if the measured spectrum is smooth.

Regularized unfolding overcomes this issue by introducing a bias (systematic error) to drastically reduce the, otherwise huge, variance (statistical error). Different strategies do exist. Here I shall discuss two of them, the χ^2 minimization and the Bayesian methods.

χ^2 minimization method

We start expressing the problem stated by eq. 3.21 as the minimization of the quantity

$$\chi^2 = \sum_{\text{refolded}} \left(\frac{y_{\text{refolded}} - y_{\text{measured}}}{\sigma_{\text{measured}}} \right)^2 . \qquad (3.27)$$

It is easy to convince ourselves that the problems of minimizing the χ^2 defined above and of solving eq. 3.21 are perfectly equivalent: this just provides us with a numerical mean to find a solution of the matrix inversion problem. To regularize the solution we shall explicitly introduce an additional term in the function to be minimized:

$$\chi^2 = \sum_{\text{refolded}} \left(\frac{y_{\text{refolded}} - y_{\text{measured}}}{\sigma_{\text{measured}}} \right)^2 + \beta \sum_{\text{unfolded}} \frac{d^2 \log y_{\text{unfolded}}}{d \log p_{\text{T}}^2}, \qquad (3.28)$$

where β is the regularization parameter. This additional term is built such that it would cancel exactly if the solution y_{unfolded} is described by a power law[4].

The regularization parameter β gives the relative strength between the two terms: if we take it to be very large the variance of the solution will be zero, but the solution itself will not depend on the measured data; conversely if we take $\beta = 0$ we are back to the unregularized solution with huge variance. One has to carefully choose a value in between, and check that the systematic uncertainty is kept at a reasonable level.

Bayesian method

A different approach to unfolding is taken in the iterative method proposed by D'Agostini [48], which contains elements of Bayesian statistics. Here one starts with a set of initial probabilities $\boldsymbol{p} = (p_1, \ldots, p_M)$ for an event to be found in each bin. In the absence of further information one can take a flat probability distribution or use the measured distribution itself. Initial estimators for $\boldsymbol{\mu}$ are

$$\hat{\boldsymbol{\mu}}_0 = n_{\text{tot}} \boldsymbol{p}_0, \tag{3.29}$$

where $n_{\text{tot}} = \sum_i n_i$ is the total observed number of entries. These estimators are updated using the rule

$$\begin{aligned} \hat{\mu}_i &= \frac{1}{\epsilon_i} \sum_{j=1}^{N} P(\text{true value in bin } i \mid \text{found in bin } j) n_j \\ &= \frac{1}{\epsilon_i} \sum_{j=1}^{N} \left(\frac{R_{ij} p_i}{\sum_k R_{jk} p_k} \right) n_j. \end{aligned} \tag{3.30}$$

Bayes' theorem formula is

$$P(C_i|E) = \frac{P(E|C_i)P(C_i)}{\sum_{l=1}^{n_C} P(E|C_l)P(C_l)}, \tag{3.31}$$

[4]Indeed in log-log a power law is described by a linear function, which has a second derivative equal to zero.

where $P(C_i)$ and $P(E_j)$ are respectively the probability of the cause i (true value in bin i) and the probability of the event j (value found in bin j). This formula has been used to derive eq. 3.30.

The procedure is iterated with the new prior probabilities taken as the solution at the previous step. In practice this is found to converge to a reasonable solution in several iterations. Continuing to iterate brings increasingly large variances and the estimators eventually approach the wildly fluctuating solution from matrix inversion.

In the Bayesian unfolding the regularization parameter is discrete and coincides with the number of iterations. However another degree of freedom is given by the initial prior.

The `RooUnfold` package

This measurement makes use of the `RooUnfold` [49] package, a `C++` library designed for ROOT [50]. It provides flexible unfolding facilities, including the handling of response matrices and efficiency.

Chapter 4

Results

4.1 Raw jet spectra

In fig. 4.1 the “raw” jet p_{T} spectra are shown. They are obtained with the Anti-k_{T} algorithm using two different radii, $R = 0.2, 0.3$. Average background subtraction is applied jet-by-jet as explained in par. 3.5.1. Jets are selected with the following prescriptions:

– $p^{\mathrm{rec}}_{\mathrm{T,jet}} > 1$ GeV/c, before average background subtraction;

– $A_{\mathrm{jet}} > 0.6 \times \pi R^2$, area calculated with the active “ghost” particle method;

– jets containing a track with $p_{\mathrm{T}} > 100$ GeV/c are rejected.

The area cut is meant to remove some extreme jets, which are most likely combinatorial. The population of tracks with $p_{\mathrm{T}} > 100$ GeV/c is expected to be dominated by fakes. However removing them before jet finding may interfere with the clustering.

The negative entries in the spectra come from combinatorial background (UE) and from the smearing of the jet p_{T} due to background fluctuations. The inclusive spectrum is indeed dominated by combinatorial background at low p_{T}. The δp_{T} distributions (figs. 3.22, 3.23) give an idea of how high in p_{T} the combinatorial jets can go.

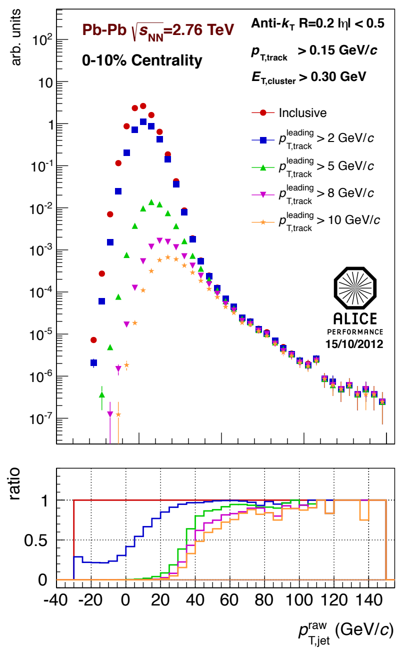

(a) $R = 0.2$.

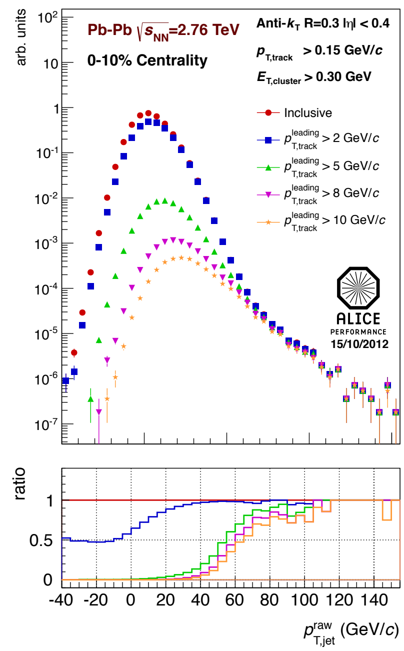

(b) $R = 0.3$.

Figure 4.1: Raw jet spectra: inclusive in red and with increasing minimum leading hadron p_T requirement in the other colors.

The two components, combinatorial jets and signal jets, are expected to have different shapes. Notwithstanding they are difficult to disentangle. While in the intermediate p_T region ($10 \lesssim p_{T,jet}^{raw} \lesssim 40$ GeV/c for $R = 0.2$ and $20 \lesssim p_{T,jet}^{raw} \lesssim 60$ GeV/c for $R = 0.3$) the relative contributions of the two components are comparable, at higher p_T jets clearly stick out form the average background. Unfolding of the background fluctuations (using δp_T distributions) should, in principle, disentangle the two components. In practice this is not achievable – at least with the current understanding of the heavy-ion background – and a bias is required for unfolding to be reasonably stable.

A minimum leading hadron p_T requirement efficiently removes most of the combinatorial jets. However it also biases the sample towards a certain fragmentation pattern, so one would want to keep it as low as possible.

4.2 $\delta p_{\rm T}$ distributions

The $\delta p_{\rm T}$ distributions for the 0-10% centrality events, are shown in fig. 4.2, where the two methods (random cones and single particle embedding, see par. 3.5.2) are compared for two different radii, $R = 0.2, 0.3$. The random cones method is used as default in the measurement, while the single particle embedding is used to determine the

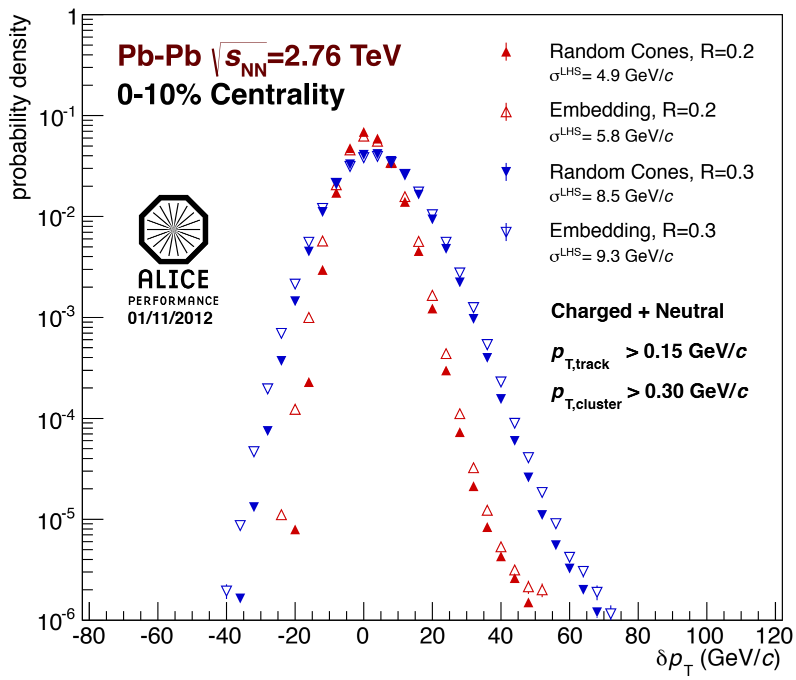

Figure 4.2: $\delta p_{\rm T}$ distributions for the 0-10% centrality class. Random cones are shown with full symbols, while single particle embedding is shown with open symbols; $R = 0.2, 0.3$ are shown respectively in red and blue.

systematic uncertainty on the background fluctuations.

What we learn from δp_{T} distributions is how much the background p_{T} density fluctuates in each event. If the average background estimation is accurate the distributions are centered at 0, as they indeed are. From them we can determine how much the jet p_{T} is smeared due to background fluctuations. For example the probability that the background fluctuates up or down by ~ 5 GeV/c in a cone of radius $R = 0.2$ is $\sim 10\%$, which means that, subtracting the average background, in 10% of the cases we will over- or under-estimate the p_{T} of the jet by ~ 5 GeV/c. As can be seen from fig. 4.2 the probabilities of higher fluctuations are several oders of magnitude smaller, but they can still have a non-negligible effect on a steeply falling spectrum.

4.3 Response matrices

In fig. 4.3 the response matrices are shown. Details about the detector response matrix are reported in par. 3.6. The background fluctuation matrix is built using random cone δp_{T} (fig. 4.2): the distribution is repeated in every slice of $p_{\mathrm{T,jet}}^{\mathrm{true}}$ (y axis), shifted along the x axis such that the 0 of the distribution coincide with the diagonal, $p_{\mathrm{T,jet}}^{\mathrm{true}} = p_{\mathrm{T,jet}}^{\mathrm{meas}}$ ("Toeplitz" matrix). Both matrices are rebinned to get a bin width of 5 GeV/c in the measured axis and 10 GeV/c in the true axis (last bin is $150 \div 250$ GeV/c). The bin width choice is driven by two aspects: statistical errors (especially at high p_{T}) and jet p_{T} resolution (see fig. 3.26). In addition, different bin widths in the two axis are needed to reduce the degrees of freedom of the unfolded spectrum, which must be less than the number of data points in the raw spectrum. While the rebinning in the measured p_{T} axis can be done without any particular assumption, in the true p_{T} axis we used the PYTHIA pp jet spectrum to have a reasonable redistribution of the contents in the merged bins. The final

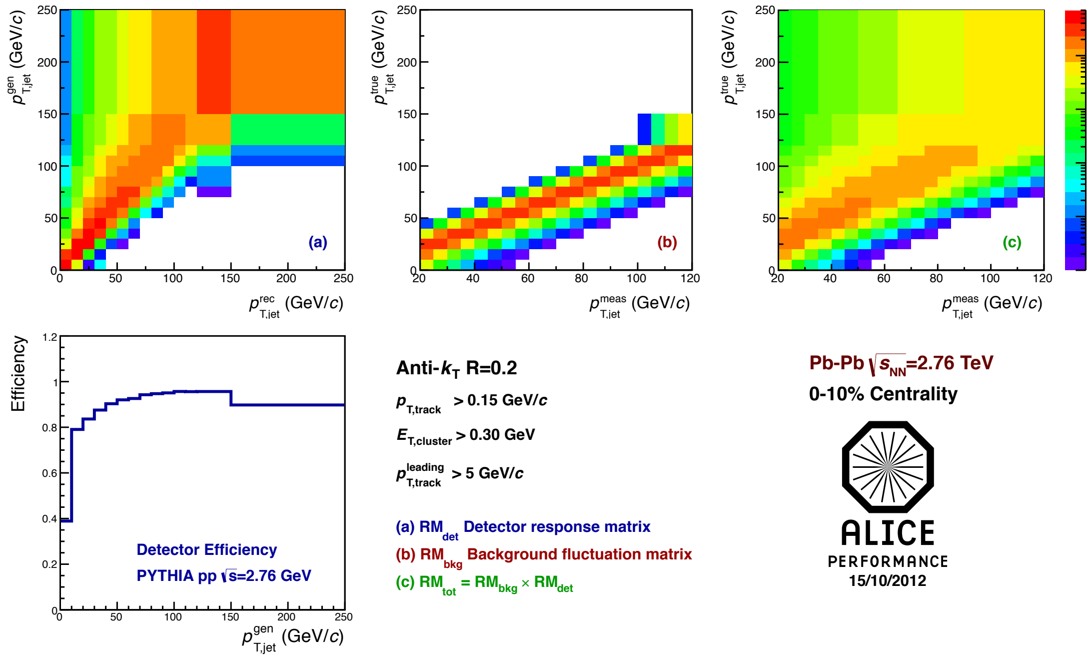

Figure 4.3: Response matrices (Anti-k_T, $R = 0.2$, $p^{\text{leading}}_{\text{T,track}} > 5$ GeV/c): (a) is obtained from a PYTHIA+GEANT3 simulation and describes the detector response to jet reconstruction (further details in par. 3.6); (b) is obtained from the random cone δp_T distribution and describes background fluctuations; (c) is the row-by-column standard matrix multiplication between (a) and (b). The jet detector efficiency is also shown.

matrix is obtained through the standard row-by-column matrix multiplication, thus including both detector and background fluctuation effects.

4.4 Unfolded spectra

The results of the Bayesian unfolding of the Anti-k_T jet spectrum with $R = 0.2$ are shown in fig. 4.4. The total response matrix (c) shown in

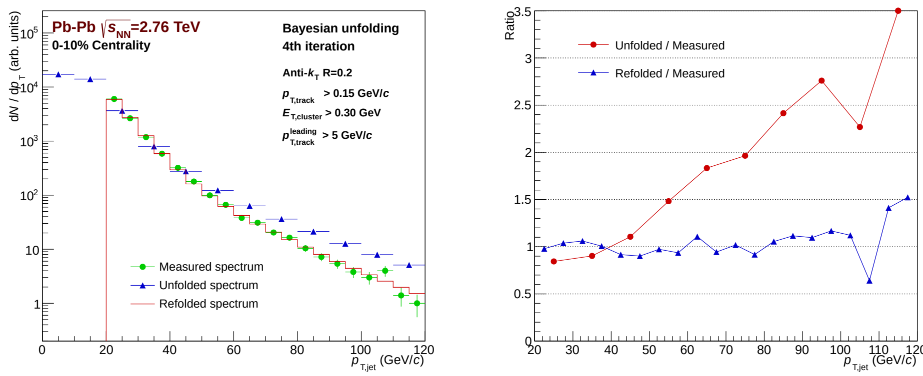

(a) *Spectra.* (b) *Ratios.*

Figure 4.4: Bayesian unfolding (4th iteration) of the Anti-k_{T} ($R = 0.2$) jet spectrum: measured spectrum (green); unfolded spectrum (blue); refolded spectrum (red).

fig. 4.3 has been employed. The "refolded" spectrum is obtained applying the same response matrix to the unfolded one. This is compared to the raw (measured) spectrum in order to check the validity of the result.

The unfolded spectrum is less steep than the raw spectrum. To further understand the two separate aspects, background fluctuations and detector response, unfolding has been performed successively in two steps, using the response matrices (a) and (b) shown in fig. 4.3. The results can be seen in fig. 4.5. Unfolding the background fluctuations (1st step) brings the spectrum down, as it ought to be. Indeed, due to the steeply falling spectrum, the net effect of a jet p_{T} smearing is to move entries from low p_{T} to higher p_{T} bins. The second step corrects for tracking inefficiency, unreconstructed particles (neutrons, K_L^0, neutrinos,...) and additional smearing due to momentum/energy resolution. The net effect of this second step is to bring the spectrum again up. So the two steps have opposite effects on the spectrum, with the detector response being the dominant one.

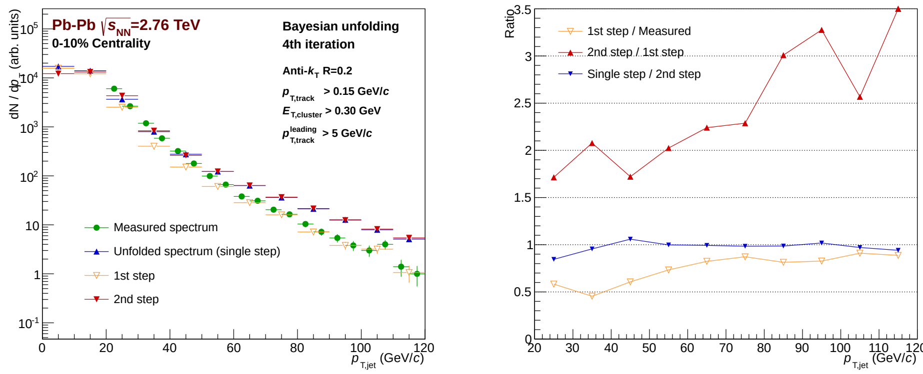

(a) *Spectra.* (b) *Ratios.*

Figure 4.5: Bayesian unfolding (4th iteration) of the Anti-k_T ($R = 0.2$) jet spectrum: measured spectrum (green); 1st step, background fluctuations (orange); 2nd step, detector response (red); single-step, total response (blue).

The Pearson coefficients are defined by the formula

$$P_{ij} = \frac{\sigma_{ij}}{\sqrt{\sigma_{ii}\sigma_{jj}}}, \tag{4.1}$$

where σ_{ij} are elements of the unfolding covariance matrix. The Pearson coefficients are defined in the range $(-1, 1)$. They have a straightforward interpretation in terms of (anti-)correlation of the bin i with the bin j:

- $P_{ij} = 1 \rightarrow$ bins are correlated;
- $P_{ij} = 0 \rightarrow$ bins are not correlated;
- $P_{ij} = -1 \rightarrow$ bins are anti-correlated.

Intermediate values give the strength of the (anti-)correlation. They are shown in fig. 4.6 for the Bayesian unfolding (4th iteration) of the Anti-k_T ($R = 0.2$) jet spectrum. Strong (anti-)correlations between distant bins are signs of a misbehaving unfolding. A strong correlation

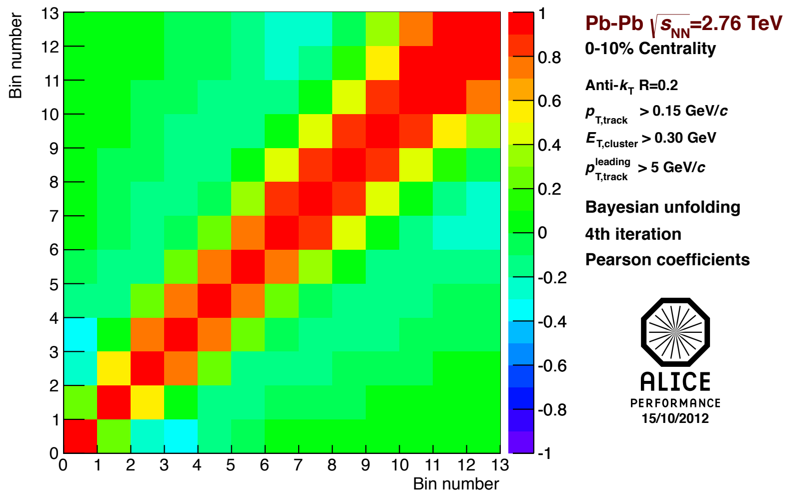

Figure 4.6: Bayesian unfolding (4th iteration) of the Anti-k_{T} ($R = 0.2$) jet spectrum: Pearson coefficients.

is of course expected within bins which are 1-2 units far apart. Anti-correlations are expected among the first bins as a result of the integral conservation constraint.

4.5 Systematic uncertainties

4.5.1 Tracking

The uncertainty of the tracking efficiency was assumed to be 5% and independent of momentum. This is a conservative number which comes from several studies on data and simulation (e.g. ITS-TPC matching efficiency, variation on the number of clusters in the TPC).

The uncertainty on the final spectrum has been calculated by removing an additional 5% of the reconstructed tracks used in the construction of the response matrix. The resulting difference in the unfolded spectra from nominal was taken to be the systematic uncertainty. This

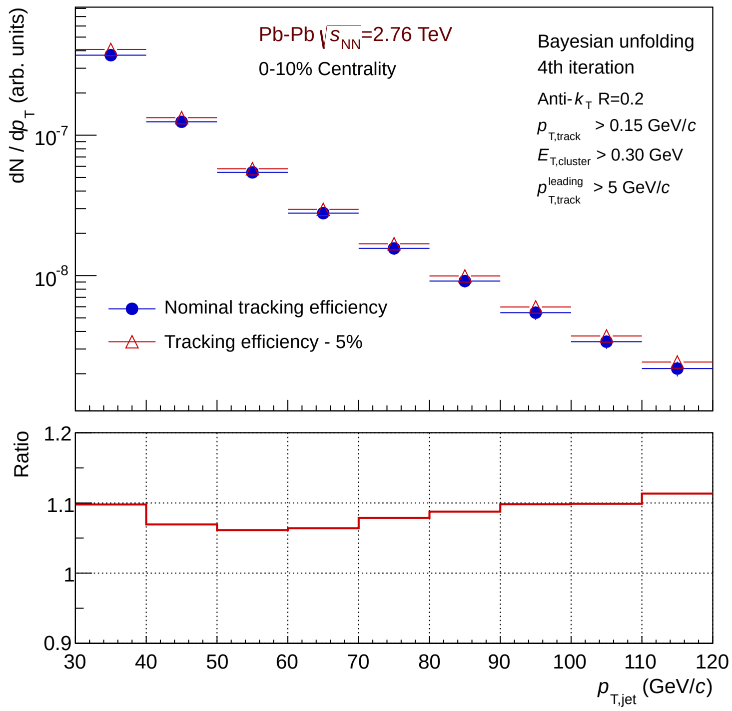

Figure 4.7: Blue: unfolded jet spectrum with nominal settings. Red: tracking efficiency reduced by 5% in the response matrix.

study is shown in fig. 4.7. It has been assumed that this distribution is symmetric, so that an increase of 5% efficiency would result in a yield variation of the same amount but of opposite sign.

In a previous analysis, performing a pp jet spectrum measurement, it was found that smearing the track momenta by 50% resulted in less than 1% difference in the final spectrum so we assumed this effect to be negligible compared to the other sources of systematic uncertainty.

4.5.2 EMCal

An exhaustive study on the systematic uncertainties for this jet measurement due to the electromagnetic calorimeter is not yet available, so we decided to use a conservative approach, quoting the maximum uncertainty we would expect after looking at previous similar measurements. For the ALICE pp jet analysis [51], the EMCal energy scale and resolution was determined using the π^0 peak and E/p distributions in both simulations and data. The jet energy scale uncertainty was found to be 2% on the cluster level and corresponded to a 3% uncertainty for the $R = 0.2$ spectrum and 4% for the $R = 0.4$ one. The energy resolution was determined to be 10% on the cluster level, which corresponded to a 1% uncertianty on the jet spectra.

The choice of the clusterizer also adds a systematic uncertainty on the measurement. In the pp analysis, the difference between the "v2" clusterizer and the "3×3" clusterizer resulted in a 5% difference on the jet spectra for $R = 0.2$ and $R = 0.4$.

Lastly there is an uncertainty due to the non-linearity correction of the calorimeter. This uncertainty is high for clusters below 300 MeV, which thus have been excluded from the analysis. The correction due to the non-linearity is applied to both data and detector-level simulation and so it is accounted for in the analysis. The systematic uncertainty in pp was determined by assuming that the EMCal had a uniform energy response in the data and then unfolding the results. This was found to result in less than a 3% uncertainty on the jet spectrum.

Adding these uncertainties together in quadrature results in a total uncertainty due to EMCal of 5.3% on the final jet p_{T} spectrum. The uncertainty due to the charged particle correction (see par. 3.3.3) was estimated separately, as it was expected to behave quite differently from the pp analysis due to the higher occupancy.

4.5.3 Charged particle correction

Since energy deposition by charged hadrons in the EMCal is an intrinsically stochastic process, an exact cluster-by-cluster correction is not

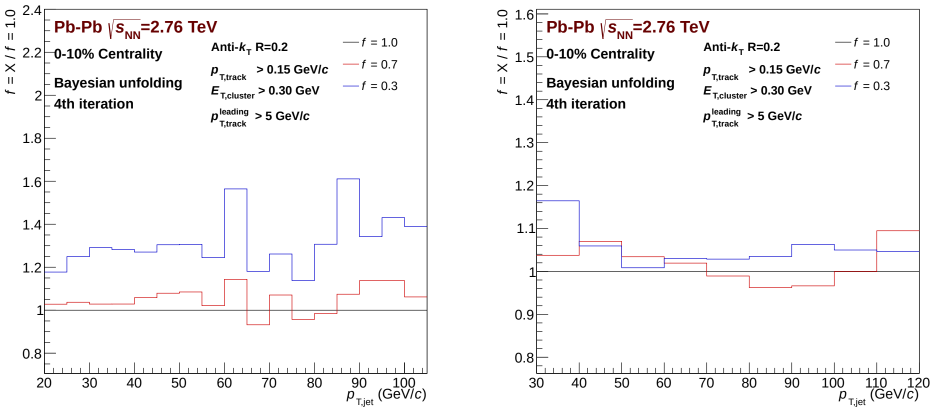

(a) *Raw spectra.*

(b) *Unfolded spectra.*

Figure 4.8: Ratio of jet spectra obtained using $f = 0.3$ (blue) and $f = 0.7$ (red) over $f = 1.0$.

achievable. In fig. 3.13 I have already shown, at cluster level, the effect of varying the fraction f of eq. 3.3. We studied what is the impact of this variations both on the raw and final (unfolded) jet spectra. Fig. 4.8 shows the results of such studies. The same correction is always applied in data and in simulation, thus partially hiding the effect in the unfolded spectra. The residual differences, in the order of 10%, have been taken as systematic uncertainty in the final jet spectrum. As none of the possible choices for f has a clear advantage, the simpler $f = 1.0$ has been chosen as default. This choice is also motivated by the fact that the same was used in the pp jet analysis.

4.5.4 Background

The two aspects of the background, average event-by-event subtraction and fluctuations, have been explored to identify sources of systematic uncertainties. Concerning the first aspect we identified the scale factor estimation (see eq. 3.15) as the most prominent source of uncertainty. To determine it, we varied the scale factor parametrization according

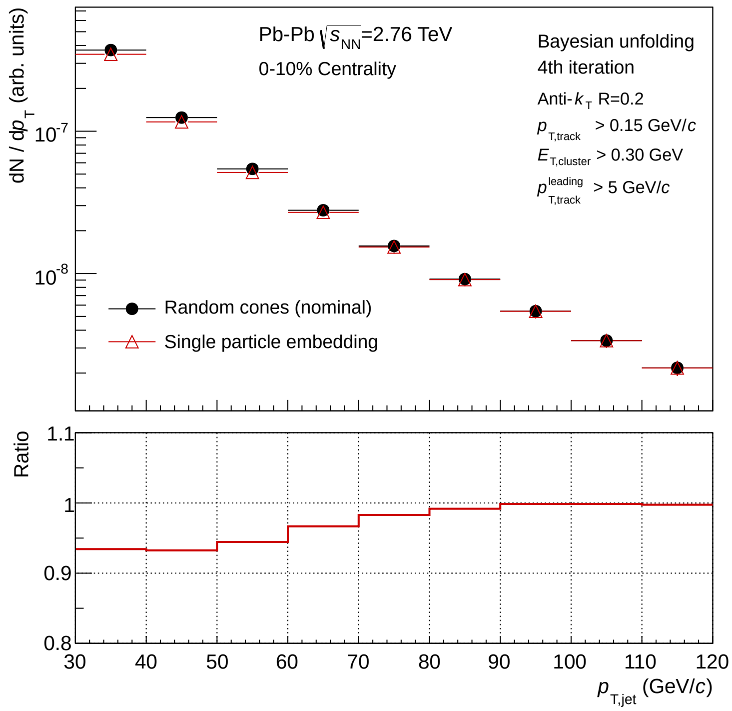

Figure 4.9: Black: unfolded jet spectrum with nominal settings (random cones). Red: single particle embedding is used instead of random cones.

to its event-by-event RMS. This gives an estimate of how "wrong" the scale factor can be with respect to the event-wise ρ calculation. This effect on the final spectrum was estimated to be 2%.

Two different methods to probe background fluctuations have been presented in par. 3.5.2, the random cone method and the single particle embedding. Both methods have advantages and disadvantages. The first method is much simpler and does not rely on any assumption about the structure of the background itself. The second method should be able reproduce more carefully the background as seen by the Anti-k_T algorithm; nevertheless embedding a high p_T particle may have an effect on the clustering which is different from what one would expect from an actual jet. Embedding an entire jet would not completely solve this issue as the problem of unambiguously matching the reconstructed jet with the probe jet would arise. The uncertainty due to the background fluctuation calculation has been estimated by unfolding the spectrum using the two methods explained before, and comparing the results (see fig. 4.9). The random cone method is the nominal choice, while the single particle embedding method gives the systematic uncertainty.

4.5.5 Unfolding

Unfolding is a process which implies some choices which are necessarily, to some extent, arbitrary. Therefore it is very important to make sure that these choices give stable results with respect to small changes, and quote the corresponding residual variations in the final result as systematic uncertainties. Four such sources of uncertainty have been identified: the number of iterations in the Bayesian unfolding (fig. 4.10), the prior choice (fig. 4.11), the p_{T} range of the raw spectrum used as input (fig. 4.12) and the p_{T} range in which the unfolded result has been constrained (fig. 4.13). The uncertainties due to small variations of these parameters, summed in quadrature, gave a total (maximum) systematic uncertainty of 14% on the final spectrum.

Table 4.1 shows a summary of all systematic uncertainties.

Table 4.1: Summary of the estimated systematic uncertainties. Some of them are p_T dependent and asymmetric. The quoted values correspond to the maximum value for each uncertainty category.

(a) *All systematic uncertainties.*

Uncertanty	% on jet spectrum
EMCal	5.3
Tracking	10
Ch. particle corr.	10
Scale factor	2
Bkg. fluctuations	5
Unfolding	14
Flow bias	< 1
Total	19

(b) *Unfolding uncertainties.*

Uncertanty	% on jet spectrum
No. of iterations	5
Measured p_T range	9
Unfolded p_T range	5
Prior choice	10
Total unfolding	14

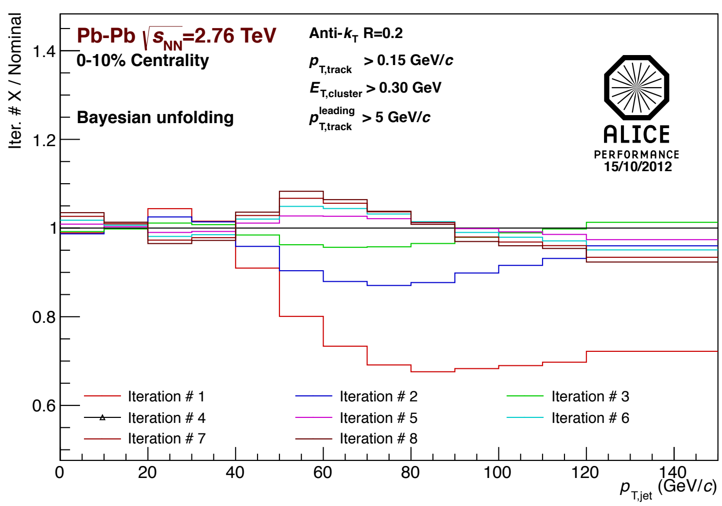

Figure 4.10: Bayesian unfolding of the Anti-k_T ($R = 0.2$) jet spectrum: from the 1st iteration to the 8th.

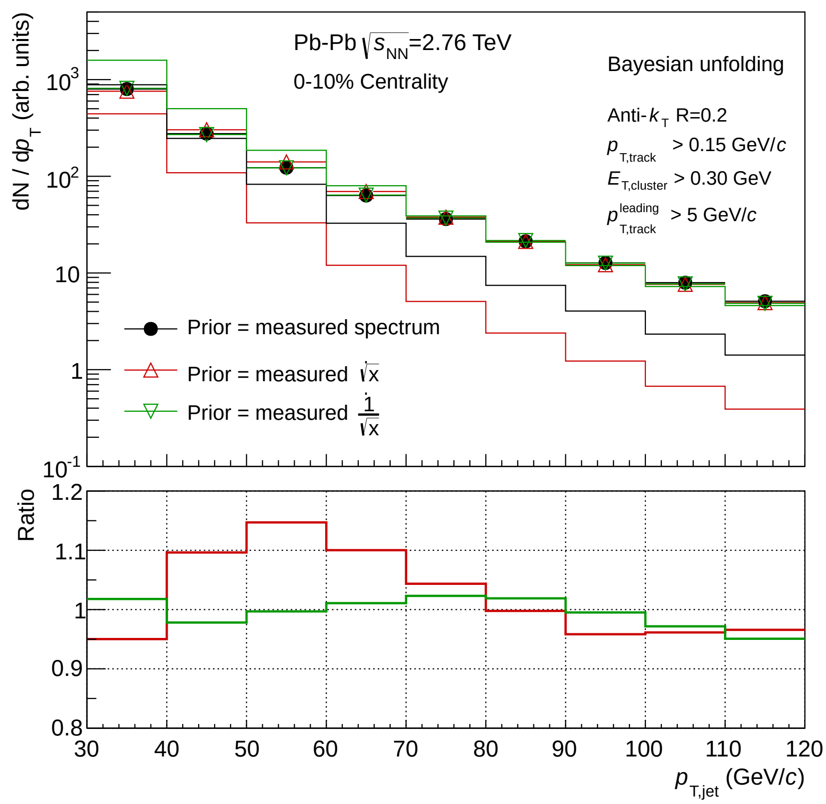

Figure 4.11: Black: unfolded jet spectrum with nominal settings (prior is the measured spectrum, 4th iteration). Red: steeper prior (7th iteration). Green: less steep prior (7th iteration).

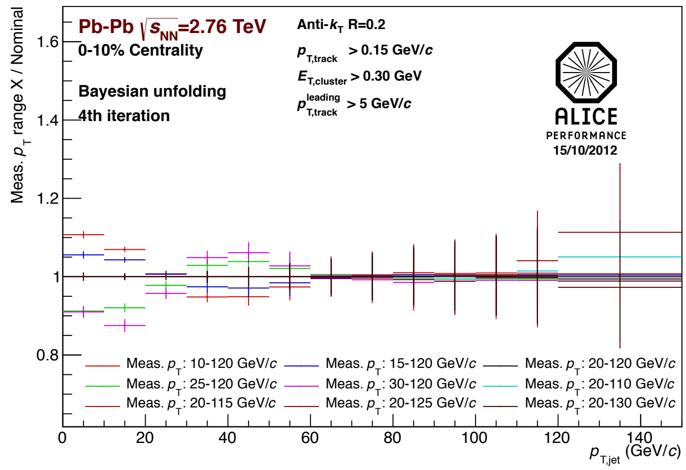

Figure 4.12: Effect of using different p_T ranges for the raw (measured) spectrum. The low cut-off choice is driven by the overwhelming combinatorial background at low p_T, while at high p_T there is lack of statistics.

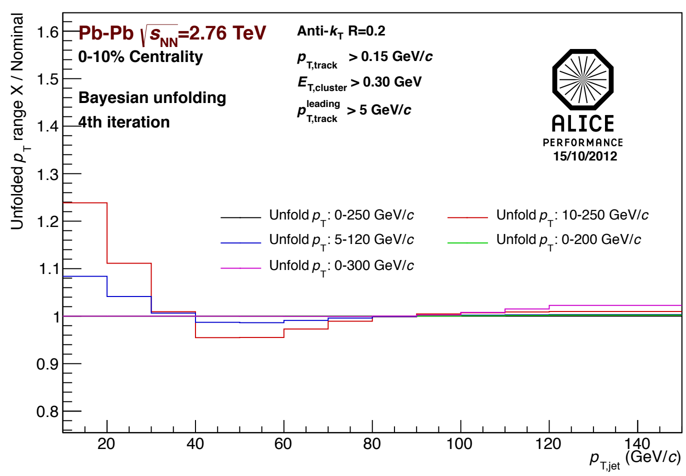

Figure 4.13: Effect of constraining the unfolded spectrum in different p_T ranges. The constrain in the nominal choice is kept to minimum (0,250). Constraining the spectrum in the low edge gives an estimate of the effect the residual contamination of combinatorial jets.

4.6 Full jet spectrum, $R = 0.2$

Fig. 4.14 shows the full reconstructed jet spectrum. Here is the summary of the measurement.

- Input particles:
  - "hybrid" tracks reconstructed with ITS and TPC detectors, $p_{\mathrm{T,track}} > 0.15$ GeV/c;
  - EMCal clusters, corrected for charged energy deposition, $E_{\mathrm{T,cluster}}^{\mathrm{subtracted}} > 0.30$ GeV/c.
- Anti-k_{T} algorithm with $R = 0.2$:
  - $A_{jet} > 0.6 \times \pi R^2$
  - $p_{\mathrm{T,track}}^{\mathrm{leading}} > 5$ GeV/c
- Average background estimated using the k_{T} algorithm and subtracted on an event-by-event basis.
- Background fluctuations estimated with random cones.
- Detector response extracted from a PYTHIA+GEANT3 simulation:
  - detector-level analysis same as data;
  - particle-level tuned to correct detector effects with $p_{\mathrm{T,const}} > 0.15$ GeV/c for both charged and neutral particles.
- Unfolded with Bayesian method, 4th iteration.

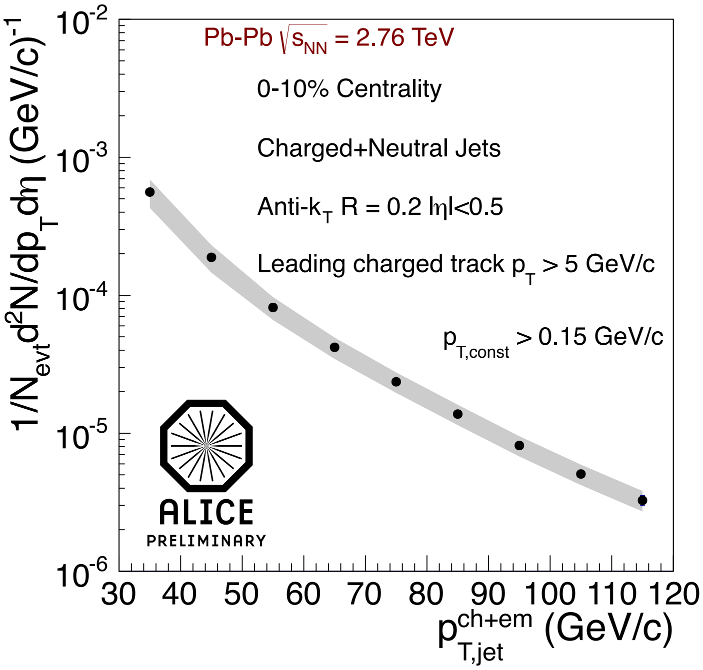

Figure 4.14: Spectrum of fully reconstructed jets in Pb–Pb collisions at $\sqrt{s_{\rm NN}} = 2.76$ TeV.

4.6.1 Leading hadron bias

The analysis have been performed also for a different leading hadron requirement, namely $p_{\rm T,track}^{\rm leading} > 10\,{\rm GeV}/c$ to better understand the effect of this requirement in the Pb–Pb jet spectrum compared to the pp measurement. This is also a preliminary study that is especially useful for larger jet radii, where a stronger bias may be needed in order to efficiently remove combinatorial jets.

Figs. 4.15a shows the two spectra with the different leading hadron biases. The ratio (fig. 4.15b) is compared with a particle-level expectation from PYTHIA (pp). Statistical and systematic uncertainties on the ratio have been computed taking into account that the two measurements come from the same data sample, and thus the uncertainties

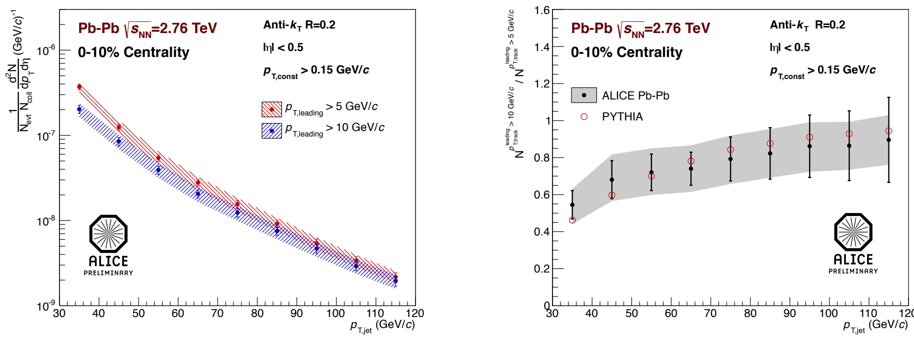

(a) *Spectra.* (b) *Ratio.*

Figure 4.15: Spectra of full reconstructed jets in Pb–Pb collisions at $\sqrt{s_{\mathrm{NN}}} = 2.76$ TeV with two different minimum leading hadron p_{T} requirements.

are partially correlated. The reasonable agreement with PYTHIA is consistent with a vacuum-like fragmentation of the jet core.

4.6.2 Nuclear modification factor

The nuclear modification factor R_{AA} is defined as follows:

$$R_{\mathrm{AA}} = \frac{\frac{1}{N_{\mathrm{evt}}}\frac{d^2N_{\mathrm{jets}}}{dp_{\mathrm{T}}d\eta}}{T_{\mathrm{AA}}\frac{d^2\sigma_{\mathrm{pp}}}{dp_{\mathrm{T}}d\eta}}. \tag{4.2}$$

The numerator in eq. 4.2 represents the measured Pb–Pb inclusive jet spectrum normalized by the number of events. In the denominator the differential jet cross section in pp collisions is scaled by the T_{AA} factor:

$$T_{\mathrm{AA}} = \frac{N_{\mathrm{coll}}}{\sigma_{\mathrm{pp}}}, \tag{4.3}$$

where N_{coll} is the number of binary nucleon-nucleon collisions for the given system (Pb–Pb at $\sqrt{s_{\mathrm{NN}}} = 2.76$ GeV/c), calculated using a Glauber model [10]. By definition, if a Pb–Pb collision could be described as a superposition of N_{coll} binary collisions this ratio would be

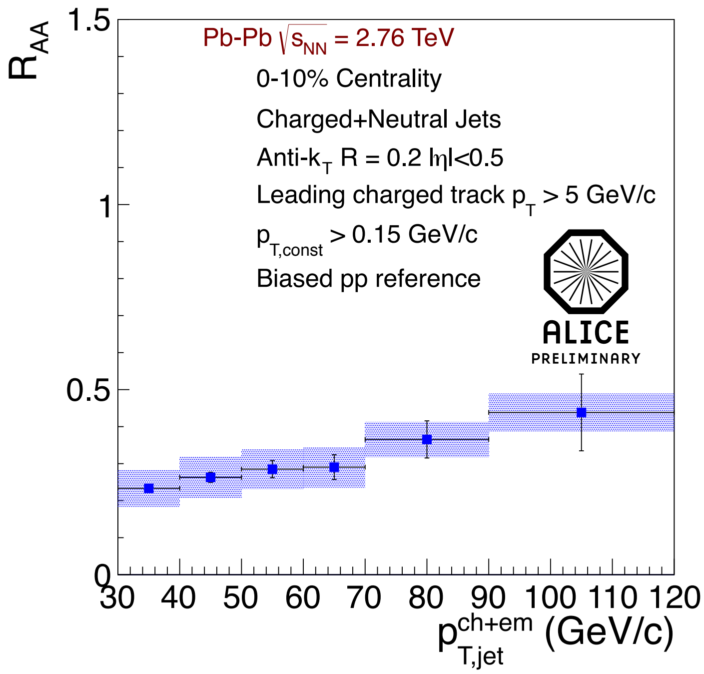

Figure 4.16: Nuclear modification factor (R_{AA}) of fully reconstructed jets in Pb–Pb collisions at $\sqrt{s_{\mathrm{NN}}} = 2.76$ TeV. The baseline spectrum is reconstructed using pp collisions at $\sqrt{s} = 2.76$ TeV. The same leading hadron bias is applied in both spectra.

one. A deviation from unity is an indication of a modification of the phenomena occuring in a collision of two nuclear systems with respect to the proton-proton collision.

A jet analysis with very similar characteristics has been previously performed by the ALICE collaboration on proton-proton collisions [51]. This analysis makes use of pp collisions at $\sqrt{s} = 2.76$ GeV/c recorded by ALICE in the first weeks of 2011. The total recorded data sample corresponds to an integrated luminosity of $\sim 11.0\ \mathrm{nb}^{-1}$, and includes minimum bias events (triggered by the V0 detector) and EMCal triggered events which allow a higher kinematical reach of the jet spectrum.

The nuclear modification factor R_{AA} is shown in fig. 4.16. It indicates a strong suppression of jets, which is on the order of 0.25, increasing slightly with p_{T}. Both a shift of the jet energy scale due to in-medium parton energy loss and a reduction of the overall yield can contribute to the observed suppression.

Conclusions

It is now more than 10 years since CERN first announced [12] "compelling" evidences of the existence of a new state of matter, which features many of the characteristics of the theoretically predicted quark-gluon plasma and is created in ultra-relativistic central heavy-ion collisions. The picture became more definite in 2005 when also RHIC experiments were able to claim [52, 53] a strong evidence of the formation of a new state of matter, characterized by the underlying quark and gluon degrees of freedom.

In the more recent years, while confirming the previous observations, both RHIC and LHC experiments are aiming at more complex measurements, to understand the details of the QGP, whose properties are still evanescent. Many of these observables make use of hard probes, which became accessible only at their higher collisional energy. Full jet reconstruction measurements are among those and have already proven to be a key mean to understand the details of the hot and dense medium created in the collision.

The reconstruction of jets in high-energy heavy-ion collisions is challenging due to the huge background coming from the underlying event. Some results, from the high p_{T} region ($p_{\mathrm{T,jet}} > 100$ GeV/c), where the separation from the combinatorial background is more straightforward, have been already reported [24, 25]. However the full reconstruction of jets in the low and intermediate p_{T} region is something completely new, although many results are now expected from all experiments in the very near future.

The first full jet reconstruction measurement from the ALICE experiment is presented here. The Anti-k_{T} algorithm, which has proven to be more suitable for the heavy-ion environment, has been employed to find jets among the particles reconstructed trough the tracking detectors (charged) and the electromagnetic calorimeter (neutral). The background is subtracted jet-by-jet; a statistical correction (unfolding) is applied to the final jet spectrum to account for the smearing due to fluctuations in the background.

The Pb–Pb jet spectrum has been compared to pp. A strong suppression, with an $R_{\mathrm{AA}} \approx 0.25$, is observed. This observation is consistent with the single particle spectrum measurements, where a strong suppression is seen at intermediate p_{T} (see fig. 1.8b and Ref. [13]). However full jet reconstruction allows a better understanding of the energy scale of the scattered partons, which suffered energy loss in the hot medium.

This measurement probably opens more question than providing definite answers. First of all we would like to understand why we observe such a strong suppression. Is this due to a shift of the energy scale or to a complete absorption of high energy partons in the medium? Where does the "lost" energy go? Is the hadron fragmentation pattern affected by the medium? Do Pb–Pb jets fragment in vacuum (as pp jets), after the parton suffered some energy loss in the medium?

To answer these and more questions experimentalists are aiming at a number of measurements, mainly looking at jet structure and correlations, where full jet reconstruction is just the first but fundamental step.

Bibliography

[1] S. Chatrchyan, V. Khachatryan, A.M. Sirunyan, and others [The CMS Collaboration], Physics Letters B **716**, 30 (2012).

[2] G. Aad, T. Abajyan, B. Abbott, J. Abdallah, and others [The ATLAS Collaboration], Physics Letters B **716**, 1 (2012).

[3] S. Bethke, Progress in Particle and Nuclear Physics **58**, 351 (2007).

[4] Johann Rafelski and Berndt Müller, Phys. Rev. Lett. **48**, 1066 (1982).

[5] K. Fanebust et al. [NA57 Collaboration], J. Phys. G **28**, 1607 (2002).

[6] F. Antinori et al. [WA97 Collaboration], Nucl. Phys. A **661**, 130 (1999).

[7] T. Matsui and H. Satz, Phys.Lett. **B178**, 416 (1986).

[8] M.C. Abreu et al. [NA50 Collaboration], Phys. Lett. B **477**, 28 (2000).

[9] G.Martínez García for the ALICE collaboration, arXiv:1106.5889v1 (2011).

[10] Michael L. Miller, Klaus Reygers, Stephen J. Sanders, and Peter Steinberg, Annual Review of Nuclear and Particle Science **57**, 205 (2007).

[11] S. Chatrchyan et al. [The CMS Collaboration], Phys. Rev. Lett. **107**, 052302 (2011).

[12] http://newstate-matter.web.cern.ch/newstate-matter/Science.html .

[13] K. Aamodt, A. Abrahantes Quintana, and other [The ALICE Collaboration], Physics Letters B **696**, 30 (2011).

[14] J. Adams and others [The STAR Collaboration], Phys. Rev. Lett. **91**, 172302 (2003).

[15] S.S. Adler and others [The PHENIX Collaboration], Phys. Rev. C **69**, 034910 (2004).

[16] J. Adams and others [The STAR Collaboration], Phys. Rev. Lett. **97**, 162301 (2006).

[17] B. Abelev, N. Arbor, G. Conesa Balbastre, and others [The ALICE Collaboration], Arxiv preprint arXiv:1210.4520v1 (2012).

[18] S. Chatrchyan, V. Khachatryan, A.M. Sirunyan, and others [The CMS Collaboration], Arxiv preprint arXiv:1210.5482v2 (2012).

[19] K. Aamodt, A. Abrahantes Quintana, and other [The ALICE Collaboration], Journal of Instrumentation **3**, S08002 (2008).

[20] Rene Bellwied for the ALICE EMCal Collaboration, Arxiv preprint arXiv:1008.0413 (2010).

[21] J Allen, C Bernard, O Bourrion, et al., http://cdsweb.cern.ch/record/1272952 (2010).

[22] M. Ploskon for the STAR Collaboration, Nuclear Physics A **830**, 255c (2009).

[23] P.M. Jacobs for the STAR Collaboration, Arxiv preprint arXiv:1012.2406 (2010).

[24] G. Aad, B. Abbott, and others [The ATLAS Collaboration], Phys. Rev. Lett. **105**, 252303 (2010).

[25] S. Chatrchyan, V. Khachatryan, A. M. Sirunyan, and others [The CMS Collaboration], Phys. Rev. C **84**, 024906 (2011).

[26] B. Abelev, N. Arbor, G. Conesa Balbastre, and others [The ALICE Collaboration], Arxiv preprint arXiv:1201.2423 (2012).

[27] Marta Verweij (for the ALICE Collaboration), arXiv:1210.8264v1 (2012).

[28] G. Hanson, G. S. Abrams, A. M. Boyarski, et al., Physical Review Letters **35**, 1609 (1975).

[29] George Sterman and Steven Weinberg, Phys. Rev. Lett. **39**, 1436 (1977).

[30] G. C. Blazey and B. L. Flaugher, Ann. Rev. Nucl. Part. Sci. **49**, 633 (1999).

[31] Gerald C. Blazey, Jay R. Dittmann, Stephen D. Ellis, V. Daniel Elvira, K. Frame, S. Grinstein, Robert Hirosky, R. Piegaia, H. Schellman, R. Snihur, V.Sorin, and Dieter Zeppenfeld, Physical Review D **45**, 1448 (2000).

[32] Gerald C. Blazey, Jay R. Dittmann, et al., arXiv:hep-ex/0005012 (2000).

[33] Gavin P. Salam and Grégory Soyez, Journal of High Energy Physics **86**, 1 (2007).

[34] Bartel, W., Becker, L., and others [The JADE Collaboration], Zeitschrift für Physik C Particles and Fields **33**, 23 (1986).

[35] S. Moretti Y. L. Dokshitzer, G. D. Leder and B. R. Webber, JHEP **9708**, 001 (1997).

[36] S. D. Ellis and D. E. Soper, Phys. Rev. D **48**, 3160 (1993).

[37] M. Cacciari, G.P. Salam, and G. Soyez, Journal of High Energy Physics **2008**, 063 (2008).

[38] M. Cacciari and G.P. Salam, Physics Letters B **659**, 119 (2008).

[39] G. Corcella et al., arXiv:hep-ph/0210213 (2002).

[40] M. Cacciari and G.P. Salam, Physics Letters B **641**, 57 (2006).

[41] Matteo Cacciari, Gavin P. Salam, and Gregory Soyez, Arxiv preprint arXiv:1111.6097 (2011).

[42] Matteo Cacciari, Gavin P. Salam, and Gregory Soyez, Journal of High Energy Physics **005**, 0804 (2008).

[43] M. Cacciari, G.P. Salam, and S. Sapeta, Journal of High Energy Physics **65**, 1 (2010).

[44] B. Abelev, N. Arbor, G. Conesa Balbastre, and others [The ALICE Collaboration], Arxiv preprint arXiv:1112.2082 (2011).

[45] K. Aamodt, B. Abelev, and others [The ALICE Collaboration], Phys. Rev. Lett. **105**, 252302 (2010).

[46] T. Sjöstrand, S. Mrenna, and P. Skands, Journal of High Energy Physics **5**, 1 (2006).

[47] GEANT3 webpage, http://wwwasd.web.cern.ch/wwwasd/geant/.

[48] G. D'Agostini, NIM A **362**, 487 (1995).

[49] RooUnfold webpage, http://hepunx.rl.ac.uk/ adye/software/unfold/RooUnfold.html.

[50] ROOT webpage, http://root.cern.ch/drupal/.

[51] R. Ma for the ALICE Collaboration, Arxiv preprint arXiv:1208.4537 (2012).

[52] J. Adams and others [The STAR Collaboration], Nuclear Physics A **757**, 102 (2005).

[53] K. Adcox and others [The PHENIX Collaboration], Nuclear Physics A **757**, 184 (2005).